Title:

Properties of snow overlying the sea ice off East Antarctica in late winter, 2007

Authors:

Takenobu Toyota[1], Robert Massom[2], Kazutaka Tateyama[3], Takeshi Tamura[4], and Alexander Fraser[5]

Submitted to Deep Sea Research II

Affiliation

1*: Institute of Low Temperature Science, Hokkaido University N19W8, Kita-ku, Sapporo, 060-0819, Japan (toyota@lowtem.hokudai.ac.jp)

*corresponding author

Tel: +81-11-706-7431 Fax: +81-11-706-7142

2: Australian Antarctic Division and Antarctic Climate and Ecosystems Cooperative Research Centre, c/o University of Tasmania, Sandy Bay, Tasmania 7001, Australia

3: Kitami Institute of Technology, Kouencho, Kitami 090-8507, Japan

4: Antarctic Climate and Ecosystems Cooperative Research Centre, c/o University of Tasmania, Sandy Bay, Tasmania 7001, Australia

5: Institute of Marine and Antarctic Studies, Antarctic Climate and Ecosystems Cooperative Research Centre, University of Tasmania, Sandy Bay, Tasmania 7001, Australia

Abstract

The properties of snow on East Antarctic sea ice off Wilkes Land were examined during the Sea Ice Physics and Ecosystem Experiment (SIPEX) in late winter of 2007, focusing on the interaction with sea ice. This observation includes 11 transect lines for the measurement of ice thickness, freeboard, and snow depth, 50 snow pits on 13 ice floes, and diurnal variation of surface heat flux on three ice floes. The detailed profiling of topography along the transects and the $d^{18}O$, salinity, and density datasets of snow made it possible to examine the snow-sea-ice interaction quantitatively for the first time in this area. In general, the snow displayed significant heterogeneity in types, thickness (mean: 0.14±0.13 m), and density (325±38 kg m^{-3}), as reported in other East Antarctic regions. High salinity was confined to the lowest 0.1 m. Salinity and $d^{18}O$ data within this layer revealed that saline water originated from the surface brine of sea ice in 20 % of the total sites and from seawater in 80 %. From the vertical profiles of snow density, bulk thermal conductivity of snow was estimated as 0.15 W K^{-1} m^{-1} on average, only half of the value used for numerical sea ice models. Although the upward heat flux within snow estimated with this value was significantly lower than that within ice, it turned out that a higher value of thermal conductivity (0.3 to 0.4 W K^{-1} m^{-1}) is preferable for estimating ice growth amount in current numerical models. Diurnal measurements showed that upward conductive heat flux within the snow and net long-wave radiation at the surface seem to play important roles in the formation of snow ice from slush. The detailed surface topography allowed us to compare the air-ice drag coefficients of ice and snow surfaces under neutral conditions, and to examine the possibility of the retrieval of ice thickness distribution from satellite remote sensing. It was found that overall snow cover works to enhance the surface roughness of sea ice

rather than moderate it, and increases the drag coefficient by about 10%. As for thickness retrieval, mean ice thickness had a higher correlation with ice surface roughness than mean freeboard or surface elevation, which indicates the potential usefulness of satellite L-band SAR in estimating the ice thickness distribution in the seasonal sea ice zone.

Keyword: Antarctic snow on sea ice, Thermal conductivity of snow, Flooding,
Snow ice formation, Air-ice drag coefficient,
Retrieval of ice thickness from satellite
Regional index term: East Antarctica

1. Introduction

The snow on the Antarctic sea ice plays important roles in the atmosphere - ocean - sea ice system in many ways. Firstly, snow modifies the role of sea ice in the surface heat budget over ice-covered seas. In winter, a vast area of the Southern Ocean (~19 x 10^6 km^2) is covered with sea ice, which has a significant influence on the heat exchange between the atmosphere and ocean on account of its high albedo (0.2-0.6) (Allison, et al., 1993) and strong thermal insulating effect (Maykut and Untersteiner, 1971). These effects are significantly enhanced by snow cover because of its higher albedo (0.6-0.9) and significantly lower thermal conductivity than sea ice (Sturm and Massom, 2010). Secondly, snow makes a major contribution to Antarctic ice growth through its transformation to snow ice. Past studies showed that snow ice accounts for 10-20 % of the total thickness for the Antarctic sea ice (Jeffries et al., 1994, 1997). Thirdly, snow cover modifies the air-ice drag coefficient by changing the surface roughness (Andreas et al., 1993). Some roughness features are associated with ice ridges, while others (such as barchan snow dunes) occur over flat (undeformed) ice areas (Massom et al., 1998). Moreover, and from the standpoint of satellite remote sensing, snow masks the surface properties of sea ice by its heterogeneous depth distribution and properties and surface flooding (Barber et al., 1998; Lubin and Massom, 2006). Recent studies have also highlighted the role of snow in the biogeochemical system as a reservoir and carrier of chemical components precipitated from the air (e.g. Nomura et al., 2010). All these factors underline the importance of better understanding snow-sea-ice interaction processes.

Although the properties of the Antarctic sea ice have been intensively investigated for a few decades, extensive detailed information on snow on the sea ice is still lacking

(Massom et al., 2001). Therefore, the individual processes of snow-ice interaction remain unclear. Observations have been especially sparse off East Antarctica. Since recent trends in surface temperature are quite different between the western and eastern Antarctica (Comiso, 2010), more detailed and continuous observation of snow properties in this region seems to be quite important.

The study by Massom et al. (1998) conducted during August 1995 around 64^{o}S 140^{o}E provided the first information on general properties of snow on sea ice in this region, regarding the distributions of snow depth, density, and salinity, and thermal conductivity. They found that each property is highly heterogeneous and the effective thermal conductivity of snow is much lower than that used for numerical sea ice models, and that flooding and subsequent snow ice formation at the snow/ice interface is ubiquitous. Similar findings came from the ARISE experiment conducted in the region 64-65.5^{o}S, 112-119^{o}E in September – October 2003 (Massom, unpublished data).

In this paper, we focus on analysis of in situ data acquired during the SIPEX experiment in East Antarctica off Wilkes Land (64-65ºS, 116-130ºE) in the late winter of 2007 (Worby et al., this volume) that allow an examination of the snow-sea ice interaction processes of flooding at the snow/ice interface, the conductive heat flux, and the air-ice drag coefficient. Knowledge of these processes and properties are considered to be key to improved understanding of the atmosphere-ice-ocean system. In addition, we examine the feasibility of the retrieval of ice thickness distribution for the snow-covered sea ice from satellite synthetic aperture radar (SAR) data, based on transect measurements. This again is an important issue to understanding the atmosphere-ice-ocean system on a global scale.

2. Measurements

The data used in this study come from 15 ice stations conducted from the R/V *Aurora Australis* in the SSIZ between September 11 and October 10, 2007. This data set is composed of three kinds of measurements: 1) snow and sea ice thickness and freeboard profiles (drill hole measurements) at 1 m intervals along 11 transect lines (mostly 200 m long but some 50-100 m long); 2) detailed vertical profiles of snow properties in 50 snow pits on 13 floes; and 3) diurnal observation of temperature profiles and surface radiative heat flux.

The snow pit measurements included detailed assessment of snow stratigraphy, snow type classification (based upon the *International Classification for Snow on the Ground* [Colbeck et al., 1990]), vertical temperature profiles, grain size, and snow sampling. Apart from two sites where no transect was laid out, snow pits were set along the transect lines at an interval of 50 m. To avoid contamination, snow pit observations were completed before the sea ice was penetrated by drilling. Snow samples were collected using a standard 3-cm-high snow sampler with a volume of 100 cm^3. After snow density was measured, the sample was melted to analyze salinity and $d^{18}O$. In this way the vertical profiles of snow density, salinity, and $d^{18}O$ were obtained. When more than one snow type was detected within a snow layer, the predominant type was recorded to represent the whole layer. One example of the measurement is demonstrated in Fig. 1. The detailed profiling of topography along the transects and the $d^{18}O$, salinity, and density datasets of snow made it possible to examine the snow-sea-ice interaction quantitatively for the first time in this area.

Diurnal observations were conducted every two hours at three ice stations on September 30- October 1, October 6, and October 7-8, when the ship remained

alongside a floe for longer than a day. These observations included measurements of vertical temperature profiles within snow, salinity and density at the basal layer, and short- and long- wave radiation on the surface using a radiometer (EKO Ltd., MR-40). The short-wave radiation was measured between 305 and 2800 nm, while the long-wave radiation between 3 and 50 μm. Due to observational difficulties in the dark, snow type classification was not included. The observation sites were located on relatively flat areas a few tens of meters away from both the transect line and the ship to avoid their effect. The snow depth was about 0.15 m at all the sites, close to the mean snow depth in this area. This observation was intended to examine the temporal evolution of temperature profiles on a diurnal time scale and its effect on the snow metamorphism because the diurnal variation of temperature becomes prominent in late winter (Fig. 2a). As will be shown later, the analysis at Station 10 (September 30 – October 1) serves to illustrate the importance of this process to snow ice formation.

In addition to the measurements on ice floes, snow samples were collected on the ship's deck during the cruise to obtain the $d^{18}O$ of intact snowfall in this area. The sampling was done mostly early in the morning just after heavy snowfall events (more than about 5 cm in depth). In total, 9 snow samples were collected in the region from 64.4°S to 65.5°S. The sampling dates are marked with solid circles in Fig.2a. The result shows that $d^{18}O$ ranges from -30.2 to -9.2 ‰ with the average being -17.6±6.4 (s.d.) ‰.

3. Results

3.1 Meteorological conditions

Time series of near-surface air temperature (Ta) and wind speed (Ws) monitored on

the ship while in the sea ice area are presented in Fig. 2. It is noted that Ta and Ws varied with high amplitude, associated with the periodical passage of cyclones. This situation is similar to the past results in this region i.e. during 1995 (Massom et al., 1998) and 2003 (Massom, unpublished data). Ta ranged from -22 to -5 ℃ with a slightly increasing trend with time. Although diurnal variability with an amplitude up to several degrees began to appear from late September, it was not so remarkable as the variation (~5 to 10 ℃) associated with cyclonic activity. Ws varied from 0 to 25 m s^{-1} and strong wind was not so persistent as had been observed in this region in mid-winter in previous years (Massom et al., 1998). However, Ws frequently exceeded 8 m s^{-1}, over which significant mechanical fragmentation and snow transport occurs (Andreas and Claffey, 1995). Therefore, it is likely that wind still had a strong influence on the snow properties in this region. Overall it can be said that the meteorological conditions during the cruise were at the early stage of transition phase from winter to spring.

3.2 General snow properties

Measurements yielded mean ice thickness, freeboard, and snow depths of 0.98±0.58 (s.d.) m (n = 1517), 0.07±0.10 m (n = 1500), and 0.14±0.13 m (n = 1756), during the study (Table 1). The high value of standard deviation relative to average indicates that both ice and snow thickness distribution was highly heterogeneous. This is similar to previous results i.e. in 1995 (Massom et al., 1998) and during ARISE 2003 (Massom, unpublished). Another notable characteristic is that the standard deviation of freeboard is larger than average, implying that negative freeboard occurs frequently. In fact, negative freeboard was observed at 239 points among 1500 (15.9 %). This result is comparable with 19 % obtained in August 1995 (Massom et al., 1998) and 15% in

September-October 2003 (Massom, unpublished data), suggesting that negative freeboards are a common feature in this region in late winter-early spring.

Based on the snow pit data set, mean salinity, density, and $d^{18}O$ were 4.36±7.42 psu (n = 197), 322±78 kg m^{-3} (n = 200), and -15.67±3.34 ‰ (n = 106), respectively. As in previous studies (Massom et al., 2001), high values of each component (density > 450 kg m^{-3}; salinity > 2 psu; $d^{18}O$ > -12 ‰) were confined to the lowest 0.1 m of snow layer, which indicates the significant influence of flooding at the snow/ice interface (Fig. 1, Fig. 3a). The mean salinity at the basal (bottom 3 cm) layer was 13.34±8.95 psu (n = 39), ranging from 0.43 to as high as 36.9 psu. As for flooding, the details will be discussed in the next section.

Regarding snow types, rounded grains were dominant (46 %), followed by faceted crystals (16 %), decomposing and fragmented precipitation particles (15 %), and depth hoar (13 %). The relatively lower fraction of depth hoar and faceted crystals, which are usually dominant snow types on Antarctic sea ice in winter (Sturm, 1998: Massom et al., 1998; Massom et al., 2001), is different from past results (Table 2). In addition, mean grain size (0.67 mm) was lower than the past results (1.5-1.7 mm). Although the mean vertical temperature gradient of -30.5 K m^{-1} exceeds the threshold for depth hoar formation (-25 K m^{-1}; Akitaya, 1974), fragmentation of snow grains due to strong wind in mid-winter may be responsible for these different properties. Thus, it is suggested that the metamorphism process has a large interannual variability. Snow properties as a function of snow types are summarized in Table 2. Slight difference in snow properties among snow types can be found. It is likely that the relatively lower values of density and higher values of $d^{18}O$ for depth hoar are attributable to the sublimation process. The difference in grain size across the snow types reflects the metamorphosis process.

For comparison, past statistical data obtained in winter off East Antarctica are listed in Table 3. Although the mean snow depth of 0.21±0.18 m in 2003 appears to be significantly large, it decreases to 0.17±0.16 m if the data on significantly rough ice floes are excluded. This roughness-based contrast is in line with ARISE observations from the same region in 2003; these showed mean snow depths of 0.36±0.22 m (n = 2947) for rough ice compared to 0.17±0.16 m (n = 1909) for smooth ice (Massom et al., 2006). With the SIPEX dataset, it is interesting to note that while mean snow depth is comparable with past results, snow density, salinity, and grain size shows a large variability. This variability mostly comes from the properties of the snow basal layer and suggests a large interannual variability in the snow-sea-ice interaction.

3.3 Basal flooding

One of the characteristic properties particularly in the Antarctic is the presence of saline and moist basal layers, which is produced by seawater flooding or capillary suction of surface brine of the ice (Sturm and Massom, 2010). If snow loading and subsequent decrease of freeboard is the major process, there should be a negative correlation between freeboard and snow salinity at the basal layer. However, Massom et al. (1998) pointed out that such an isostatic balance process can explain the flooding by only 20 %. Also from our analysis it is shown that basal snow salinity is negatively correlated with freeboard, but only weakly (Fig. 3b). It is likely that high salinity (> 10 psu) for the 0.3 m freeboard originates from surface brine of the ice. Besides snow loading, seawater flooding occurs due to deformation in the inner region and due to wave and swell penetration process in the marginal ice zone. Thus the flooding process is complicated and has not been well understood yet due to lack of data.

Here as a preliminary step, we attempt to identify the origin of the saline water in the snow with $d^{18}O$ and salinity data. The available $d^{18}O$ data were obtained at 32 snow pit sites. As shown in Fig. 3a, relatively high salinity (> 2 psu) is confined to the basal 0.1 m, similar to the results reported in the Antarctic other regions (Massom et al., 2001) and sub-polar regions (e.g. Okhotsk Sea; Toyota et al., 2007). Noticeably, salinity even higher than surface seawater salinity (34.3 psu from CTD measurement) was observed at some points. To examine the origin of the salinity more explicitly, basal salinity data were plotted against $d^{18}O$ in Fig. 3c. In this figure, the end member of snow lies in the range of -17.58±6.42 ‰ for $d^{18}O$ and 0 psu for salinity from the observational result of snowfall. As for surface seawater, we have no available data concerning $d^{18}O$ in this region, unfortunately. However, referring to the values in the other Antarctic regions (-1.1 ‰ for the Bellingshausen and Amundsen Seas and -0.3 to -0.5 ‰ for the Weddell and Ross Seas; Jeffries et al., 1994), we adopt the range between -1.1 and -0.3 ‰. When we connect the upper and lower limits of these two end members, it is found that there are 5 points which deviate significantly from the area intervened by these two lines (Fig. 3c). This implies that at these points the salinity cannot be explained only by the mixture of seawater and snow and involved brine with much higher salinity. In addition to these 5 points, one point near the line with a salinity of 25.1 psu and $d^{18}O$ of -7.19 ‰ is classified into this category because the salinity at a depth of 3-6 cm was as high as 41.3 psu. Since at these 6 sites the snow/ice interface temperature (T_i) was -4.6 to -16.8 ^{o}C, the surface brine salinity is estimated to be 80 to 200 psu, according to Weeks and Ackley (1986). Although we do not have the data, $d^{18}O$ of brine is considered to be close to that of seawater. Therefore the mixture of brine and snow seems to successfully explain the 6 deviated points in Fig. 3c.

Consequently, it is concluded that brine was the major origin of high salinity at 6 snow pit sites among 32 (20%), and seawater flooding prevailed at the remaining sites (80%). However, it should be noted that even within the intervened area in Fig. 3c some points may be explained by mixture of brine and snow. Therefore the estimate of 20 % is a lower limit. It may be interesting to compare this result with that for the sub-polar sea ice, e.g. the Okhotsk sea ice, for which it was concluded that the high salinity at the basal layer was caused totally by seawater flooding (Toyota et al., 2007).

There are two major ways in which brine salinizes snow: one is by flooding through brine channels associated with the depression of the ice surface, and the other is capillary suction of brine. Except for one sample where T_i= -4.6 ^{o}C and freeboard = 0 m, T_i was always below -8 ^{o}C at the 5 points. This indicates that the ice was impermeable (Crocker and Wadhams, 1989) and the capillary suction was more important than flooding through brine channels. Interestingly, it was found that at one site (Station 1) brine came up to the height of 6-9 cm. Since capillary suction of brine usually comes up to a few centimeters at most (Alvarez-Aviles et al., 2008), additional processes seems to have worked. Direct inclusion of frost flower which had formed on thin ice may be one possibility.

Basal wet layers caused by flooding sometimes evolve into snow ice. For the understanding of the processes of snow ice formation, the mechanism of releasing heat from the wet flooded layer is important (Ackley et al., 2008). Regarding this matter, we will discuss later in section 3.4.3.

3.4 Thermal properties

3.4.1 Thermal conductivity of snow

Here we estimate the thermal conductivity of snow as a preliminary step to understanding snow-sea-ice interaction from a thermodynamic perspective. The conductive heat flux through the snow-sea-ice medium involves the heat transport from the ocean to atmosphere, which enable determination of the thermodynamic growth rate of sea ice if ocean heat flux is known. If the basal snow layer is wet, conductive heat flux within snow removes heat from the basal wet layer, leading to the formation of snow ice. The vertical conductive heat flux through the snow (F_s) is obtained from the Fourier heat conduction equation:

$$F_s = k_{bulk} \frac{\partial T}{\partial z} \cong k_{bulk} \cdot \frac{T_s - T_i}{H_s} \qquad (1)$$

where k_{bulk} is the bulk effective thermal conductivity of snow and T_s and T_i are the snow surface and snow/ice interface temperature, respectively, and H_s is the full depth of snow cover. This equation assumes nearly linear profiles of temperature so as not to store heat within the snow. In our case, this assumption holds mostly true with the average of $(T_s\text{-}T_i)/H_s$ being -30.5 K m^{-1} (n = 46). In the snow-sea-ice system, k_{bulk} is a particularly important parameter because it essentially determines the degree of insulation of the snow-sea-ice medium. Based on the measurement with a needle probe, it was shown from past researches that mean k_{bulk} measured in snow pits ranged from 0.112 to 0.138 W m^{-1} K^{-1} on West Antarctic pack ice (Sturm et al., 1998) and was 0.164 W m^{-1} K^{-1} on East Antarctic pack ice (Massom et al., 1998). Both estimates are only about half the value of 0.31 W m^{-1} K^{-1} that is typically used in large-scale sea ice models (e.g. Semtner, 1976). Wu et al. (1999) showed with a coupled atmosphere-sea ice model that the use of 0.16 W m^{-1} K^{-1} instead of 0.31 W m^{-1} K^{-1} for k_{bulk} results in the reduction of mean ice thickness by about 0.2 m in the Antarctic. This implies that it is crucial to

use an appropriate value of k_{bulk} in sea ice and climate models, in order to accurately both simulate current conditions and predict future sea ice characteristics under a climate change scenario. Therefore, based on our measurements, we again examine the values of k_{bulk} to confirm these previous results and then estimate F_s with the measured value.

To calculate k_{bulk}, we used the following equation on the assumption that conductive heat flux within snow is constant and only vertical at any depth:

$$\frac{1}{k_{bulk}} = \sum_{i=1}^{n} \frac{1}{k_i} \cdot \frac{H_{si}}{H_s} \qquad (2)$$

where k_i and H_{si} are the effective thermal conductivity and thickness of the *i-th* snow layer, respectively. While Massom et al. (1998) and Sturm et al. (1998) used the constant values of k_i assigned to each snow type, we calculated it as a function of snow density from the following formula of Sturm et al. (1997) because the variability in density was quite large even for the same snow type:

$$k_i = 0.132 - 1.01\rho + 3.233\rho^2 \quad \text{for} \quad 0.156 \le \rho \le 0.6 \qquad (3)$$

where ρ is snow density in g cm^{-3}. Equation (2) and (3) were applied to all the snow pit data to obtain k_{bulk} at each snow pit. The estimated k_{bulk} ranged from 0.066 W m^{-1} K^{-1} where faceted crystals were dominant to 0.400 W m^{-1} K^{-1} where snow was mostly saline and wet, with the average being 0.149 ± 0.069 W m^{-1} K^{-1} (n = 36). By comparison, this value is comparable with the results obtained by Massom et al. (1998) and Sturm et al. (1998). To check our method, we also calculated k_{bulk} using k_i assigned to each snow type (Sturm et al., 1997) and confirmed that the estimated k_{bulk} was almost the same (0.141 W m^{-1} K^{-1} on average). Thus based on the thermal conductivity measured with the needle probe (Sturm et al., 1997), it was confirmed that the real effective bulk

thermal conductivity of snow is significantly smaller than the value typically used in numerical models. However, it should be noted that Sturm (personal communication) reports that several groups (including him) are revisiting needle probe measurements in snow trying to ascertain if there is a systematic low-bias within the measurements that was previously undetected.

3.4.2 Conductive heat flux

Using the values of k_{bulk}, T_s, T_i, and H_s measured at each snow pit, vertical conductive heat flux through the snow (F_s) was calculated from equation (1). The results averaged for each ice station are summarized in Table 1. Although F_s has a large variation, ranging from 1.0 to 11.0 W m^{-2}, as a whole there is a decreasing trend with time, corresponding to the increasing trend of air temperature (Fig. 2a). The mean F_s is 4.9±4.1 W m^{-2}, comparable with the previous results for the East Antarctic (6.2 W m^{-2}; Massom et al., 1998) and for the West Antarctic (2.9 to 9.2 W m^{-2}; Sturm et al., 1998). Although our result coincided with the past researches, another problem is raised. This relates to the fact that the estimated F_s is significantly smaller than the conductive heat flux within the ice (F_{ice}) which was calculated similarly from the heat conduction equation:

$$F_{ice} = k_{ice} \cdot \frac{T_i - T_f}{H_i} \qquad (4)$$

where k_{ice}, T_f, and H_i are the effective thermal conductivity of sea ice (2.0 W m^{-1} k^{-1}; Yen, 1981), the freezing temperature of seawater (-1.8 ^{o}C), and ice thickness measured in situ, respectively. The calculated F_{ice} was 15.8±10.3 W m^{-2} on average, which is about three times larger than F_s. In the ‘zero-layer’ version sea ice model of Semtner (1976) that has

been adopted by many numerical models, F_{ice} is calculated with T_s, H_s, and H_i on the assumption that conductive heat flux is continuous at the snow-sea-ice interface, *i.e.* $F_s = F_{ice}$. In the model, the ice growth rate is determined with the estimated value of F_{ice}. Therefore, the considerable discordance of F_s and F_{ice} is not a negligible problem. This issue will be discussed later in section 4.1.

3.4.3 Diurnal variation of thermal conditions

The results obtained in the previous sections were based on data only obtained at one point in time. As shown in Fig. 2, however, the diurnal variation in meteorological conditions begins to be more prominent in late winter. Therefore, the temporal evolution of the snow and ice properties is an important issue to consider. Here we examine the effect of the diurnal variation of vertical temperature profile within the snow on F_s and thus on the snow-sea-ice interaction. Time series of temperature at each snow layer are shown in Fig. 4a for Station 10, in Fig. 4b for Station 13, and in Fig. 4c for Station 14. Among the three figures, the variation of vertical temperature profiles in Fig. 4a is particularly prominent. It is interesting to note that while T_s had a large variation, T_i remained almost constant during the period. This implies that while F_s had a large diurnal variation, F_{ice} remained largely unchanged. To examine this explicitly, time series of F_s and F_{ice} were calculated similarly from (1) and (4); these are shown in Fig. 5a. In calculating F_{ice}, H_i was represented here by the mean ice thickness along the transect. It is noticeable that F_s rapidly increased and eventually exceeded F_{ice} around 23:00, associated with the decrease of T_s. This suggests that the heat source existed within the snow layer. On the other hand, the temperature variation in Fig. 4b and Fig. 4c was not as prominent as in Fig. 4a. Accordingly, F_s showed no significant variation,

with its value being less than half that of F_{ice} (Fig. 5b and Fig. 5c).

Next, we examine what caused the differences observed at Stations 10, 13 and 14. The probable factors are the presence/absence of a wet basal layer and clear sky conditions. At Station 10, the basal 3-cm thick layer was wet with a salinity of as high as 26-30 psu (Fig. 6a) and a density of ~500 kg m^{-3}(Fig. 6b), while at Station 13 and 14, wetness was much less with the salinity and density of the basal layer being 1-2 psu and 300-340 kg m^{-3}, respectively. As for the sky condition, cloud dissipated at Station 10 around 21:00 (LST) and the clear skies lasted until 06:00 the next morning, while it was fine to cloudy at Station 13 and totally cloudy at Station 14. The possible scenario is as follows: cloud dissipation around 21:00 at Station 10 reduced downward long-wave radiation significantly, leading to a rapid decrease in T_s. Because of wet conditions, on the other hand, T_i remained near constant, which induced a significant increase in F_s. In contrast, and at Station 14 where the sky remained overcast throughout the night, only a slight change in T_s occurred, and T_i varied accompanied by the change of T_s due to lack of basal wetness. Therefore, F_s remained almost constant. At Station 13 the surplus heat flux absorbed at the surface due to solar radiation also precluded the decrease of T_s.

Our data support the above supposed scenario. At Station 10 the downward long wave radiation decreased from 270 W m^{-2} at 17:40 to 234 W m^{-2} at 21:40. If the decrease of this flux (= 36 W m^{-2}) was used to cool the surface 0.1 m layer of snow, the decreasing rate of T_s is estimated to be 1.9 ^{o}C hr^{-1} (= 36 W m^{-2}/ (325 kg m^{-3} x 0.1 m x C_s), where C_s is the heat capacity of snow (2.12 x 10^3J kg^{-1} K^{-1}; Mellor, 1977). This value almost coincides with the observed decrease of T_s by 8.3 ^{o}C in 4 hours (Fig. 4a). The decrease of T_s led to an increase in F_s of about 15 W m^{-2}. On the other hand, at Station 14, the upward long-wave radiation (269 W m^{-2} on average) was stable, and

almost balanced by the downward long-wave radiation during the night (259 W m^{-2}). In this scenario, the key seems to be the variation of downward long-wave radiation caused by clouds. At Station 10, the large F_s ended at 06:00 the next morning when clouds covered the sky again (Fig. 5a). Since the net short-wave radiation was only 17 W m^{-2} at that time, it is reasonable to assume that the abrupt increase in T_s was brought about by the increase of clouds, rather than by any change in solar radiation.

The calculation of F_s and F_{ice} also allows us to estimate the rate of snow ice formation from a saturated basal snow layer. When F_s eventually exceeded F_{ice}, the difference of the fluxes (F_s-F_{ice} ~10 W m^{-2}) is considered to contribute to the release of the latent heat to produce snow ice within the basal layer. On this assumption, the freezing rate (*FR*) is estimated to be 0.6 cm day^{-1} from the following equation:

$$FR = \frac{F_s - F_{ice}}{\rho \cdot L_f} = \frac{10 Wm^{-2}}{500 kgm^{-3} \times 3 \cdot 10^5 Jkg^{-1}} \qquad (5)$$

where ρ is the density of snow and L_f is the latent heat of fusion of ice (Yen, 1981). If this value of *FR* is applied, it would take 5 days for a wet snow basal layer 3 cm thick to become frozen. Unfortunately, we could not validate this value because F_s decreased the next morning. Even so, there was some evidence for snow ice formation. The salinity of the basal layer showed a decreasing trend (Fig. 6a), possibly caused by brine drainage associated with freezing. Moreover, the snow density showed a slight increasing trend from 500 to 560 kg m^{-3} over the nighttime (Fig. 6b). Although F_s and thus *FR* depends largely on H_s and T_s, the values of H_s (~0.14 m) and T_s (~ -12 ^{o}C) at Station 10 were both very close to the average (0.14 m and -11.6 ^{o}C) observed in this region during SIPEX. Therefore, our estimation may be regarded as being nearly representative of this region at this time of the year. Interestingly, the estimated *FR* is almost comparable with

the ice growth rate at the floe bottom (~0.5 cm day^{-1}) which was calculated from F_{ice}. This indicates the importance of snow ice formation as well as the bottom freezing to the thermodynamic ice growth process.

3.5 Air-ice drag coefficient

To examine the snow-sea-ice interaction from a dynamical aspect, we here analyze the transect data to determine how snow cover modifies the ice surface and then estimate its effect on the air-ice drag coefficient. It is known that when the 5-m wind speed exceeds 8 m s^{-1}, significant transport of unconsolidated dry snow takes place to rework the surface (Andreas and Claffey, 1995). This phenomenon sometimes produces depositional features such as dunes, barchans, and drift aprons (Sturm and Massom, 2010). Andreas and Claffey (1995) stressed the significant effect of these depositional features on air-ice drag coefficient. Since the wind speed frequently exceeded 8 ms^{-1} (Fig. 2b), it is expected that the redistribution of snow depth in response to the wind is considerable and may produce unique properties in this region. To the authors' knowledge, however, the measurements of the air-ice drag coefficient in the Antarctic has been concentrated on the Weddell Sea so far (e.g. Andreas et al., 1984; Martinson and Wamser, 1990; Andreas and Claffey, 1995; Fisher and Lytle, 1998), and there are no available data in East Antarctica. The air-ice drag coefficient is an important parameter for determining the dynamical interaction between the atmosphere and sea ice, and accurate regional estimates are therefore required from the in situ observations. We focus here on whether snow works to enhance or moderate the roughness of sea ice, and how much effect snow cover has on the air-ice drag coefficient.

To do this, we used the following empirical formula by Banke et al.(1980) which

was derived from various Arctic sites to relate the neutral stability air-ice drag coefficient referenced to a height of 10 m (C_{DN10}) with a property of the ice surface:

$$10^3 C_{DN10} = 1.10 + 0.072\zeta \qquad (6)$$

where ζ is the root mean square (rms) surface elevation in cm at wavelengths less than 13 m. This is calculated by integrating the Fourier wave number spectrum, *X(k)*, of the surface topography.

$$\zeta^2 = \int_{k0}^{\infty} X(k)dk. \qquad (7)$$

where k is the wave number and k_0 is the lowest wave number that was set to be 0.5 radians m^{-1} on the assumption that only small-scale features affects the drag coefficient. By calculating ζ for the freeboard and snow surface elevation from the 10 transect datasets, we estimated C_{DN10} for a hypothetical snow-free ice surface and the snow covered surface, respectively, to examine the effect of snow cover on C_{DN10}. For comparison, rms roughness (a standard deviation) was also calculated for each surface. So far, this approach has been tested in Antarctica in the Weddell Sea by Andreas et al. (1993) and Fisher and Lytle (1998) in the similar way, and it was ensured that the drag coefficient derived from equations 6 and 7 almost coincided with the valued measured by other methods in the Weddell Sea, ranging between 1.2×10^{-3} and 2.2×10^{-3}. While Andreas et al. (1993) concluded that C_{DN10} for a bare sea ice surface tended to be larger than that for a snow-covered surface, indicating that the ice surface is slightly rougher than the snow surface, Fisher and Lytle (1998) showed the opposite tendency. Here, our purpose is to apply this method to the East Antarctic sea ice where first-year ice is dominant and compare the result with that from the Weddell Sea where heavily ridged multi-year ice is also present.

Typical snow and ice surface profiles measured along a 200 m long transect line at

Station 14 are shown in Fig. 7a. To see the dominant scale of the surface features, the wave number spectrum was calculated for snow (Fig. 7b) and ice (Fig. 7c) surfaces. What is evident from these figures is that the peaks of the spectrum appear at about 10 and 18 m in both surfaces. Also in Fig. 7a the snow and ice surface profiles look relatively well correlated at these scales, suggesting that the ice surface features remain on the snow surface. After examining all 10 transects, it was found that the dominant spectrum peak appeared at 3 to 67 m for both snow and ice surfaces, with the average being 34 m for snow and 26 m for ice. To compare the surface roughness, scatter plots of the rms roughness for snow and ice surface at each site are shown in Fig. 8a. It is shown that they are well correlated (R = 0.87) and the roughness of the snow surface is 1.6 times greater than that of the ice surface. All these results indicate that the snow surface "retains" the ice surface features to some extent with a slight increase in the characteristic scale, and enhances the roughness- rather than reduces it. These results are consistent with those obtained in the Bellingshausen, Amundsen, and Ross Seas by Sturm et al. (1998). The latter study also showed from transect measurements that the structural length for the snow surface was 3-70 m, and that the surface roughness for snow was 1.9 times larger than for ice.

To examine the effect of the enhanced roughness on the air-ice drag coefficient, we calculated the value of C_{DN10} for snow and ice surfaces at each site. The results are plotted in Fig. 8b, and show that the two values are highly correlated (R = 0.93) and that the value of C_{DN10} for snow surface (average: 1.39×10^{-3}) is slightly larger (by about 10%) than for ice surface (1.29×10^{-3}). Both values are comparable with those in the Weddell Sea, reported by Andreas et al. (1993) and Fisher and Lytle (1998). As for the tendency of C_{DN10} between ice and snow surface, our data support the result of Fisher

and Lytle (1998) rather than that of Andreas et al. (1993). As Andreas and Claffey (1995) pointed out, however, C_{DN10} significantly depends on the wind direction relative to the orientation of surface features such as ridges and dunes. Further data are required to ascertain the wider applicability of this result.

4. Discussion

4-1. Discontinuity of conductive heat flux

In section 3.4.2, we pointed out that F_s was significantly smaller than F_{ice} during SIPEX. Since the basal growth rate of sea ice is calculated from F_{ice} in models, the replacement of F_{ice} with F_s would result in underestimating ice thickness. To date, this issue has been addressed by Sturm et al. (2002). They attributed this mismatch partly to the two- and three-dimensional geometry of snow and ice, and suggested that the complex geometry produces non-uniform heat flux distribution and areas of concentrated heat loss on the snow surface. Yet, at the same time, they also admitted that other non-conductive heat transfer mechanisms should work to compensate this discrepancy. From our analysis, it was found that even for the relatively flat ice station (Station 8) where H_i= 0.36±0.02 m and H_s= 0.09±0.04 m, F_s (1.2 W m^{-2}) was significantly lower than F_{ice} (17.8 W m^{-2}). Therefore, such a geometric effect does not seem to necessarily explain this mismatch. Here, we address this issue from the perspective of its impact on numerical models.

To look more closely, F_s is plotted against F_{ice} for all the snow pit sites in Fig. 9a. It is found in this figure that not only the averages of these two fluxes but also the correlation of individual data are only moderately good (R = 0.52). If we adopt the value k_{bulk} = 0.3 used in the models, mean F_s slightly increases to 9.6±6.3 W m^{-2}. This

is still smaller than F_{ice} and the correlation is not improved (R = 0.41). This indicates that the assumption of $F_s = F_{ice}$ in the model is basically invalid. If this is the case, then a more complicated method is required to estimate the exact value of F_{ice} and thus the ice growth rate. Here, we check the validity of the method to estimate ice growth rates based on the 'zero-layer' version sea ice model of Semtner (1976). In this model, F_{ice} is calculated on the assumption $F_s = F_{ice}$ as follows:

$$F_{ice\_model} = \frac{k_{snow} k_{ice}}{k_{ice} H_s + k_{snow} H_i} \cdot (T_f - T_s) \qquad (8)$$

where k_{snow} and k_{ice} are the thermal conductivities of snow and sea ice, set to be 0.3 and 2.0 W m^{-1} K^{-1}, respectively, after Semtner (1976). This value was then compared with the observed value of F_{ice} calculated from (4). The result is shown in Fig. 9b. Surprisingly, it is found that these two fluxes are well correlated (R = 0.92) and the absolute values of F_{ice_model} also became closer to F_{ice} (rmse = 5.7 W m^{-2}). If we use 0.40 W m^{-1} K^{-1} for k_{snow}, F_{ice_model} becomes further closer to F_{ice} (rmse = 4.9 W m^{-2}). This result implies that although the real k_s is about half the value typically used in models, a larger value of k_s in the model actually provides a good approximation of ice growth rate.

How can we interpret this result? Our speculation is as follows: the difference of 10.9 W m^{-2} between F_{ice} and F_s is mainly used for sublimation of ice at the snow/ice interface. Moreover, vapor produced by sublimation probably moves upward through the pore spaces between snow grains. If this is the case, then the rate of sublimation is estimated to be 0.36 mm day^{-1}. Accordingly, a void space of a few cms thickness is expected to be produced at the snow/ice interface over several months in winter. In fact, void spaces near the snow basal layer were often observed (Fig. 10). The fact that

sublimation associated with depth hoar near the basal layer is active may also support this idea. As F_{ice} becomes larger, sublimation at the interface would become more active, leading to large discrepancy between F_s and F_{ice} (Fig. 9a). It is likely that the discrepancy was effectively reduced by using a larger value of k_s. Thus non-conductive heat transfer which Sturm et al. (2002) considered as another option but dismissed at that time can possibly explain the discrepancy.

4-2. Retrieval of sea ice thickness distribution from satellite SAR data

Finally, we raise the possibility of estimating the thickness of snow-covered ice from satellite synthetic aperture radar (SAR) data. As shown before, snow on sea ice works to modify the surface properties of sea ice. Our interest is to examine whether it is still possible to estimate the ice thickness distribution under snow-covered conditions and which parameter is most effective for it - particularly in the Antarctic SSIZ, where modification by snow seems to be large due to the presence of various types of sea ice. We approach this issue using the transect data.

This issue is important also from the aspect of the global monitoring of sea ice thickness. Regarding the retrieval of ice thickness from satellite remote sensing, the possibility has been investigated using passive microwave sensors (SSM/I, AMSR-E), SARs, radar altimeters (ERS-1&2/ RA and CryoSat II), and laser altimeters (ICESAT/ GLAS) (Lubin and Massom, 2006). For thin ice (<0.2 m), passive and active microwave sensors are potentially useful based on the fact that the dielectric property determined by surface brine volume depends on ice thickness (e.g. Martin et al., 2004; Wakabayashi et al., 2004). Estimates of the thickness of perennial ice (~ a few meters thick) can be derived from measurements of floe freeboard obtained with radar and laser altimeters,

on the assumption of isostatic balance and with independent knowledge of snow thickness and density (e.g. Laxon et al., 2003; Kwok et al. 2004). However, estimation of the thickness of first-year ice of intermediate thickness is still an unresolved issue. Although L-band SAR was shown to be a candidate for the remote measurement of seasonal sea ice thickness in the Sea of Okhotsk (Japan) because of the relationship between surface roughness and ice thickness (Toyota et al., 2009), validation in various other regions is still required. The detailed transect measurement provide a good opportunity for this.

Here, we simply calculated the correlation coefficients between mean ice thickness and the possible surface parameters measured at each ice station (Table 4). This allows us to deduce which satellite sensor is most effective to extract ice thickness information at a scale of about 100 m. It is found from Table 4 that the highest correlation (0.86) is provided by the standard deviation of freeboard (i.e. ice surface roughness), followed by mean snow depth (0.82) and mean surface elevation (0.78). Not surprisingly, the correlation with either T_s or T_i is poor. Basal snow salinity has a significant but only moderate negative correlation, probably related to mean freeboard. It is noticeable that a low correlation (0.43) was estimated for mean freeboard, which is a key factor enabling derivation of perennial ice thickness from satellite radar altimeter data (Laxon et al., 2003).

To examine the relationship more closely, scatter plots for several components are shown in Fig. 11. Fig. 11a shows that ice surface roughness is almost linearly correlated with ice thickness. This can be interpreted as follows. In the SSIZ, pressure ridge formation (pile-up) is a key process by which the ice thickens (e.g. Worby et al., 1996; Toyota et al., 2007). It therefore follows that the degree of surface roughness correlates

with ice thickness. With these factors in mind, SAR backscatter is strongly determined by surface roughness, and the snow cover is largely transparent to SAR unless wet (Lubin and Massom, 2006). As discussed by Dierking and Busche (2006), L-band SAR (wavelength = 24 cm) appears to be more sensitive to ice surface roughness than C-band (6 cm), because the wavelength more closely approximates the scale of surface roughness. This supports the result of Toyota et al. (2009).

On the other hand, Fig. 11b and Fig. 11c show the mean freeboard and surface elevations are also highly correlated with ice thickness except for one or two sites where well-developed pressure ridges were present. Although altimeters are a primary means of determining sea ice thickness, the problem of measurement accuracy therefore remains. In the case of mean freeboard, while measurement accuracy of satellite altimeters is 0.11 m (Laxon et al., 2003), a difference of only a few centimeters in freeboard leads to a difference in ice thickness of about 0.5 m (Fig. 11b). It is interesting to note that mean snow depth is highly correlated with ice thickness (Fig. 11d). This is probably because the maximum depth of snow is restricted depending on ice thickness due to isostatic balance and any excess of snow is constantly transformed to snow ice (Sturm et al., 1998). However, while large-scale snow depth estimates are currently derived from passive microwave data (Markus and Cavalieri, 1998), validation is still needed for accurate estimation (Worby et al., 2008). Consequently, we conclude from our transect data that L-band SAR shows potential for estimating ice thickness distribution in the Antarctic SSIZ.

5. Conclusions

Detailed ice and snow thickness measurements along transect lines, snow pit

observations, and diurnal monitoring observations conducted during SIPEX, have revealed information on general snow properties and some aspects of snow-sea-ice interaction in East Antarctica during late winter.

The snow displayed significant heterogeneity in types, thickness (mean: 0.14±0.13 m), and density (325±38 kg m^{-3}), as was the case in 2003 (Massom, unpublished data) and as reported in other Antarctic regions (Massom et al., 2001). Comparison with past results obtained in 1991-95 and 2003 showed significant interannual variability in dominant snow type, density, and salinity, although mean snow depth was nearly constant. High salinity was confined to the basal 0.1 m of snow layer, as reported in other Antarctic regions (Massom et al., 2001) and sub-polar regions (the Sea of Okhotsk ; Toyota et al., 2007).

To examine the flooding process at the snow/ice interface, $d^{18}O$ data were used to carry out a first examination of the flooding process in this region. Salinity and $d^{18}O$ data from the basal snow layer revealed that saline water originated from the surface brine of sea ice at 20 % of the sites sampled, while seawater flooding prevailed at the remaining 80 %.

To examine the snow-sea-ice interaction from a thermodynamic perspective, bulk thermal conductivity of snow (k_{bulk}) was estimated from the vertical profiles of snow density, following the method of Sturm et al. (1997) and Massom et al. (1998). The conductive heat flux within snow (F_s) was also calculated using the estimated k_{bulk} and measured temperature profile data. As a result, it was found that k_{bulk} was 0.15 W K^{-1} m^{-1} on average, only half the value typically used in numerical sea ice models, and mean F_s (4.9 W m^{-1} K^{-1}) was only one third of F_{ice} (15.8 W m^{-1} K^{-1}). However, it turned out that a higher value (0.3 to 0.4 W K^{-1} m^{-1}) of k_{bulk} is preferable for estimating ice

growth in current numerical models, probably due to the sublimation effect at the interface.

From diurnal measurement of the snow vertical temperature profile and surface radiative flux, it was shown that, in the presence of a wet basal layer, the diurnal variation of T_s directly accompanied that of F_s and can contribute to snow ice formation when F_s eventually exceeds F_{ice}, and that downward long-wave radiation due to changes in cloud coverage played an important role in this process. From the heat budget calculation, the rate of snow ice formation was estimated to be 0.6 cm day^{-1}, comparable with the basal growth rate of the sea ice. This result confirms the importance of snow-ice formation, as well as bottom freezing to the overall sea ice growth processes.

Topographic properties of the snow and ice surfaces were analyzed, using the detailed transect data, and the effect of snow cover on C_{DN10} was estimated using the empirical formula of Banke et al. (1980). The results show that the overall snow cover retains the features of ice surface at decameter scales and works to enhance the surface roughness of sea ice rather than reduce it, and increases C_{DN10} by about 10 % from 1.29 x 10^{-3} to 1.39 x 10^{-3} on average. This almost coincided with the result obtained in the Weddell Sea where both first- and multi-year ice are present (Fisher and Lytle, 1998).

Finally, we used the transect dataset to evaluate the possibility of retrieving the sea ice thickness distribution from satellite data. A conclusion is that mean ice thickness is best correlated with ice surface roughness, which indicates the potential usefulness of satellite L-band SAR as a means of estimating the ice thickness distribution in the Antarctic SSIZ from satellite – as is the case in the Sea of Okhotsk (Toyota et al., 2009).

In summary, although some key aspects of snow-sea-ice interaction were revealed from our study, additional in situ measurements are needed for validation purposes and

to determine and monitor interannual inter-seasonal variability. Clearly, further continuous observation is desirable.

Acknowledgments

The authors deeply appreciate the support given by the crew and scientists onboard the R/V *Aurora Australis* during SIPEX. Special thanks are given to the chief scientists, Dr. A. Worby, for his dedicated assistance. Discussion with Akihiro Hachikubo and Hiroyuki Enomoto were helpful. The International Space Science Institute (Bern, Switzerland) is also acknowledged for supporting this study via project #137. This work was supported partly by JSPS KAKENHI 18510003 & 21510002 [Grant-in-Aid for Scientific Research (C)] and partly by the Australian Government's Cooperative Research Centre program through the ACE CRC, and contributes to AAS Project 3024.

Reference

Ackley, S. F., M. J. Lewis, C. H. Fritsen, H. Xie, 2008. Internal melting in Antarctic sea ice: Development of “gap layers”, *Geophys. Res. Lett.*, 35, L11503, doi:10.1029/2008GL033644.

Akitaya, E., 1974. Studies on depth hoar. *Contribution from the Institute of Low Temperature Science*, Series A, 26, 1-67.

Allison, I., R.E. Brandt, S.G. Warren, 1993. East Antarctic sea ice: Albedo, thickness distribution, and snow cover. *Journal of Geophysical Research*, 98(C7), 12,417-12,429.

Alvarez-Aviles, L., W.R. Simpson, T.A. Douglas, M. Sturm, D. Perovich, F. Domine, 2008. Frost flower chemical composition during growth and its implications for aerosol production and bromine activation. *Journal of Geophysical Research*, 113, D21304, doi:10.1029/2008JD010277.

Andreas, E.L., W.B. Tucker III, S.F. Ackley, 1984. Atmospheric boundary-layer modification, drag coefficient, and surface heat flux in the Antarctic marginal ice zone. *Journal of Geophysical Research*, 89(C1), 649-661.

Andreas, E.L., M.A. Lange, S.F. Ackley, P. Wadhams, 1993. Roughness of Weddell Sea ice and estimates of the air-ice drag coefficient. *Journal of Geophysical Research*, 98(C7), 12,439-12,452.

Andreas, E.L., K.J. Claffey, 1995. Air-ice drag coefficients in the western Weddell Sea. 1. Values deduced from profiles measurements. *Journal of Geophysical Research*, 100(C3), 4821-4831.

Banke, E.G., S.D. Smith, R.J. Anderson, 1980. Drag coefficients at AIDJEX from sonic anemometer measurements, In *Sea Ice Processes and Models*, edited by R.S.

Pritchard, pp. 430-442, University of Washington Press., Seattle.

Barber, D.G., A.K. Fung, T.C. Grenfell et al., 1998. The role of snow on microwave emission and scattering over first-year sea ice. *IEEE Trans. Geosc. Rem. Sens.*, 36(5), 1750–1763.

Colbeck, S. C., E. Akitaya, R. Armstrong, H. Gubler, J. Lafeuille, K. Lied, D. McClung, E. Morris, 1990. *The International Classification for Seasonal Snow on the Ground*. The International Commission on Snow and Ice of the International Association of Scientific Hydrology, and the International Glaciological Society, 23pp.

Comiso, J.C., 2010. Variability and trends of the global sea ice cover. In *Sea Ice*, 2nd Edition, edited by D.N. Thomas and G.S. Dieckmann, Wiley-Blackwell, Oxfod, UK, pp. 205-246.

Crocker, G.B., P. Wadhams, 1989. Modelling Antarctic fast-ice growth. *J. Glaciol.*, 35, 3-8.

Dierking, W., T. Busche, 2006. Sea ice monitoring by L-band SAR: An assessment based on literature and comparisons of JERS-1 and ERS-1 imagery. *IEEE Trans. Geosci. Remote Sensing*, 44, No.2, 957-970.

Fisher, R., V.I. Lytle, 1998. Atmospheric drag coefficients of Weddell Sea ice computed from roughness profiles. *Ann. Glaciol.*, 27, 455-460.

Jeffries, M.O., R.A. Shaw, K. Morris, A.L. Veazey, H.R. Krouse, 1994. Crystal structure, stable isotopes (d18O), and development of sea ice in the Ross, Amundsen, and Bellingshausen seas, Antarctica. *Journal of Geophysical Research*, 99 (C1), 985-995.

Jeffries, M. O., A. P. Worby, K. Morris, W. F. Weeks, 1997. Seasonal variations in the properties and structural an isotopic composition of sea ice and snow cover in the

Bellingshausen and Amundsen Seas, Antarctica. *J. Glaciol.*, *43*, 138-151.

Kwok, R., H.J. Zwally, D. Yi, 2004. ICESat observations of Arctic sea ice: First look, *Geophys. Res. Lett.*, Vol. 31, L16401, doi:10.1029/2004GL020309.

Laxon, S., N. Peacock, D. Smith, 2003. High interannual variability of sea ice in the Arctic region, *Nature*, 425, 947-950.

Lubin, D., R.A. Massom, 2006. *Polar Remote Sensing. Volume 1: Atmosphere and Polar Oceans*, Praxis/Springer, UK and Germany, 756 pp.

Markus, T., D.J. Cavalieri, 1998. Snow depth distribution over sea ice in the Southern Ocean from satellite passive microwave data. In *Antarctic Sea Ice: Physical Processes, Interactions and Variability*, ed. by M.O. Jeffries. American Geophysical Union, Washington, D.C. (*Antarct. Res. Ser., 74*), 19-39.

Martin, S., R. Drucker, R. Kwok, B. Holt, 2004. Estimation of the thin ice thickness and heat flux for the Chukchi Sea Alaskan coast polynya from Special Sensor Microwave/Imager data, 1990-2001. *Journal of Geophysical Research*, 109, C10012, doi: 1010.29/ 2004JC002428.

Martinson, D.G., C. Wamser, 1990. Ice drift and momentum exchange in winter Antarctic pack ice. *Journal of Geophysical Research*, 95(C2), 1741-1755.

Massom, R.A., V.I. Lytle, A.P. Worby, I. Allison, 1998. Winter snow cover variability on East Antarctic sea ice. *Journal of Geophysical Research*, 103(C11), 24,837-24,855.

Massom, R.A., H. Eicken, C. Haas, et al., 2001. Snow on Antarctic sea ice. *Reviews of Geophysics*, 39, 413-445.

Massom, R. A., Worby, A. P., Lytle, V. I., Markus, T., Allison, I., Scambos, T., Enomoto, H., Tateyama, K., Haran, T., Comiso, J. C., Pfaffling, A., Tamura, T., Muto, A., Kanagaratnam, P., Giles, B., 2006. ARISE (Antarctic Remote Ice Sensing

Experiment) in the East 2003: Validation of satellite derived sea ice data products. *Ann. Glaciol.*, 44, 288-296.

Maykut, G.A., N. Untersteiner, 1971. Some results from a time-dependent thermodynamic model of sea ice. *Journal of Geophysical Research,* 76(6), 1550–1575.

Mellor, M., 1977. Engineering properties of snow. *J. Glaciol.*, 19(81), 15-65.

Nomura, D., J. Nishioka, M.A. Granskog, A. Krell, S. Matoba, T. Toyota, H. Hattori, K. Shirasawa, 2010. Nutrient distributions associated with snow and sediment-laden layers in sea iceof the southern Sea of Okhotsk. *Marine Chemistry*, 119, 1-8.

Semtner, A.J., 1976. A model for the thermodynamic growth of sea ice in numerical investigations of climate. *J. Phys. Oceanogr.*, 6, 379-389.

Sturm, M., R.A. Massom, 2010. Snow and Sea Ice. In D. Thomas and G. Dieckmann (editors), *Sea Ice*, 2nd Edition, Wiley-Blackwell, Oxford, pp. 153-204.

Sturm, M., J. Holmgren, M. Koenig, K. Morris, 1997. The thermal conductivity of seasonal snow. *J. Glaciol.*, 43 (143), 26-41.

Sturm, M., K. Morris, R. Massom, 1998. The winter snow cover of the West Antarctic pack ice: its spatial and temporal variability. In *Antarctic Sea Ice: Physical Processes, Interactions and Variability*, ed. by M.O. Jeffries. American Geophysical Union, Washington, D.C. (*Antarct. Res. Ser., 74*), 1-18.

Sturm, M., D.K. Perovich, J. Holmgren, 2002. Thermal conductivity and heat transfer Through the snow on the ice of the Beaufort Sea. *Journal of Geophysical Research*, 107, doi:10.1029/2000JC000409.

Toyota, T., Takatsuji, S., Tateyama, K., Naoki, K., Ohshima, K.I., 2007. Properties of sea ice and overlying snow in the southern Sea of Okhotsk,

Journal of Oceanography, 63, 393-411.

Toyota, T., K. Nakamura, S. Uto, K.I. Ohshima, N. Ebuchi, 2009. Retrieval of sea ice thickness distribution in the seasonal ice zone from airborne L-band SAR. *Int. J. Remote Sens.*, 30, No. 12, 3171-3189.

Wakabayashi, H., T. Matsuoka, K. Nakamura, F. Nishio, 2004. Polarimetric characteristics of sea ice in the Sea of Okhotsk observed by airborne L-band SAR. *IEEE Trans. Geosci. Remote Sensing*, 42, No. 11, 2412-2425.

Weeks, W.F., S.F. Ackley, 1986. The growth, structure, and properties of sea ice. In *The Geophysics of Sea Ice*, edited by N. Untersteiner, Plenum Press, New York, US, 9-164.

Worby, A.P., M.O. Jeffries, W.F. Weeks, K. Morris, R. Jana, 1996. The thickness distribution of sea ice and snow cover during late winter in the Bellingshausen and Amundsen Seas, Antarctica, *J. Geophys., Res.*, 101, 28,441-28,455.

Worby, A.P., T. Markus, A.D. Steer, V.I. Lytle, R.A. Massom, 2008. Evaluation of AMSR-E snow depth product over East Antarctic sea ice using in situ measurements and aerial photography. *Journal of Geophysical Research*, 113, C05S94, doi:10.1029/2007JC004181.

Wu, X., W.F. Budd, V.I. Lytle, R.A. Massom, 1999. The effect of snow on Antarctic sea ice simulations in a coupled atmosphere-sea ice model. *Climate Dynamics*, 15, 127-143.

Yen, Y.C., 1981. Review of thermal properties of snow, ice, and sea ice. *CRREL Rep.*, 81-10, 1-27.

Figure captions:

Figure 1. Typical vertical profiles of snow measured at Station 3.

(a) Snow type (b) Temperature (c) Density (d) Salinity (e) $d^{18}O$.

Note that the snow basal layer has higher values of salinity, density, and $d^{18}O$, indicating the flooding effect.

Figure 2. Meteorological conditions along the cruise track while in the ice area (from September 11 to October 10).

Time series of (a) air temperature; and (b) wind speed

Solid circles in Fig.2a denote the dates when snow samples were collected on the ship's deck for the measurement of $d^{18}O$, implying that there was heavy snowfall on the previous day.

Figure 3. Salinity plots as a function of

(a) height above the snow/ice interface;

(b) sea ice freeboard of sea ice (only basal layer salinity is plotted); and

(c) $d^{18}O$ (only basal layer salinity is plotted).

Figure 4. Time series of snow temperature at each layer, obtained during the period of diurnal observation, at (a) Station 10 (September 30 – October 1);

(b) Station 13 (October 6); and (c) Station 14 (October 7-8)

Figure 5. Time series of conductive heat flux within snow (F_s) and ice (F_{ice}), estimated from diurnal observation, at (a) Station 10 (September 30 – October 1);

(b) Station 13 (October 6); and (c) Station 14 (October 7-8)

Figure 6. Time series of (a) basal layer salinity and (b) basal layer density observed during the diurnal observations at Station 10.

Figure 7. An example of topographic features obtained from a transect measurement at Station 14. (a) Profiles of snow and ice surfaces elevations. Power spectra for (b) snow surface and (c) ice surface.

Figure 8. Scatter plots between ice and snow surfaces for (a) roughness and (b) air-ice drag coefficient under neutral conditions. Regression lines are $(snow\ roughness) = 1.57 \times (ice\ roughness)$ for Fig. 8a and $C_{DN10}\ (snow) = 1.09 \times C_{DN10}\ (ice) + 0.02$ for Fig. 8b.

Figure 9. Scatter plots of the conductive heat flux within ice (F_{ice}) against
(a) conductive heat flux within snow (F_s) and
(b) the value calculated from the '0-layer version' of numerical ice models (Semtner, 1976)

Figure 10. Sample photos taken at Station 5 where depth hoar was observed at the basal layer, showing the active sublimation and void space so produced at the snow/ice interface. (a) photo of a snow pit
(b) magnified photo of the frame in Fig.10a

Figure 11. Scatter plots of mean ice thickness against
(a) standard deviation of freeboard (*i.e.* ice surface roughness);
(b) mean surface elevation (*i.e.* height of snow surface);
(c) mean freeboard (*i.e.* height of ice surface); and
(d) mean snow depth

Table 1. The results of observation and estimated heat flux within snow and sea ice

Ice station No.	Date (2007)	Length of transect (m)	H_i (m)	F_b (m)	H_s (m)	T_i (^oC)	Snow pit number	Snow density (kg m^{-3})	k_{bulk} (W m^{-1} K^{-1})	dT/dz (K m^{-1})	F_s (W m^{-2})	F_{ice} (W m^{-2})
St.1	Sep.11	100	0.82	0.04	0.18	-7.6	3	342	0.200	34.4	6.2	18.8
St.2	Sep.12-13	200	1.03	0.03	0.20	-9.7	5	338	0.181	39.1	7.1	8.1
St.3	Sep.14	100	0.99	0.05	0.17	-10.6	3	284	0.112	46.7	5.3	13.1
St.4	Sep.17	-	-	-	0.24	-	1	308	0.128	13.6	1.7	12.7
St.5	Sep.18	200	0.71	0.04	0.09	-12.7	5	319	0.167	48.3	8.3	30.1
St.6	Sep.21	200	1.15	0.10	0.02	-11.1	5	-	0.133	33.7	4.5	25.0
St.7	Sep.22	-	-	-	-	-	1	154	0.056	42.0	2.3	-
St.8	Sep.25-26	195	0.36	0.01	0.09	-3.9	5	289	0.099	12.6	1.2	17.8
St.9	Sep.28	50	2.22	0.14	0.44	-6.5	1	374	0.211	7.6	1.6	-
St.10	Sep.30-Oct.01	200	0.69	0.03	0.09	-8.0	5	361	0.196	56.2	11.0	23.8
St.11	Oct.03	100	1.06	0.29	0.22	-6.6	3	306	0.125	8.4	1.0	9.3
St.12	Oct.05	-	-	-	-	-	-	-	-	-	-	-
St.13	Oct.06	200	1.04	0.07	0.15	-5.5	6	306	0.119	22.9	1.9	8.1
St.14	Oct.07-08	200	1.14	0.04	0.22	-5.5	7	321	0.146	16.1	2.4	7.3
St.15	Oct.10	-	-	-	-	-	-	-	-	-	-	-
All	mean	1745	0.98	0.07	0.14	-8.0	50	325	0.148	30.5	4.9	15.8
	s.d.		0.58	0.10	0.13	3.6		38	0.067	20.5	4.1	10.3

(*) H_i: mean ice thickness, F_b: mean freeboard, H_s: mean snow depth, T_i: mean snow/ice interface temperature
k_{bulk} : mean bulk thermal conductivity of snow, dT/dz: mean vertical temperature gradient of snow which was calculated from $(T_s-T_i)/H_s$.
F_s: mean conductive heat flux of snow, F_{ice}: mean conductive heat flux of ice
At St.12 and 15 only ice core sampling was done. At St.9 F_{ice} is blank because a snow pit was set 10m away from the transect.
At St.6 snow density is blank because snow cover was too thin for the measurement of density. There k_{bulk} was obtained from snow type, according to Sturm et al. (1997).

Table 2. Statistics of snow properties for each snow type category.

Type	Fraction (%)	Grain size (mm)	Density (kg m^{-3})	Salinity (psu)	$d^{18}O$ (permil)
PP	0.2	1.50	-	-	-
DS	14.9	0.26±0.12	283±109	1.88±3.82	-16.47±2.04
RG	45.9	0.43±0.29	327±64	2.17±4.95	-17.55±1.97
FC	15.6	0.44±0.19	311±42	2.60±4.30	-17.02±1.55
DH	12.9	1.50±0.89	316±35	4.25±3.99	-15.54±2.72
WG	7.9	1.95±1.28	358±111	12.56±9.38	-12.07±2.22
IL	1.8	-	-	-	-
WC	0.7	-	-	-	-
Total	100.0	0.67	325±38	4.36±7.44	-15.46±3.32

(*) PP: Precipitation particles DS: Decomposing and fragmented precipitation particles
RG: Rounded grains FC: Faceted crystals DH: Depth hoar
WG: Wet grains IL: Ice layer WC: Wind crust
(After "The International Classification for Seasonal Snow on the Ground" (Colbeck et al., 1990))

Table 3. Comparison with the past results in winter

	Year	Longitude (E)	Mean	Range	Number of data
Snow depth (m)	Oct.-Nov. 1992	62-102	0.13	0.00-0.76	68
	Sep.-Oct. 1994	75-150	0.15	0.05-1.40	113
	Aug. 1995	138-141	0.13	0.02-0.70	794
	Sep.-Oct. 2003	109-118	0.21	0.00-1.03	2475
	Sep.-Oct. 2007	115-130	0.14	0.0-1.04	1756
Snow density ($kg\ m^{-3}$)	Aug. 1995	138-141	360	120-760	170
	Sep.-Oct. 2003	109-118	306	110-839	215
	Sep.-Oct. 2007	115-130	322	154-539	200
Grain size (mm)	Sep.-Oct. 1994	75-150	1.7	0.05-4.0	17
	Aug. 1995	138-141	1.6	0.01-10	167
	Sep.-Oct. 2003	109-118	1.6	0.1-5.0	165
	Sep.-Oct. 2007	115-130	0.7	0.1-5.0	123
Snow bulk Salinity (psu)	Sep.-Oct. 1994	75-150	8.8	0.1-66.4	41
	Aug. 1995	138-141	8.5	0.1-54.4	202
	Sep.-Oct. 2003	109-118	4.22	0.1-38.1	197
	Sep.-Oct. 2007	115-130	4.36	0.0-41.3	197
Basal layer salinity (psu)	Aug. 1995	138-141	17	0.1-54.4	76
	Sep.-Oct. 2003	109-118	13.31	0.10-38.1	46
	Sep.-Oct. 2007	115-130	13.34	0.43-36.9	39

Table 4. Correlation coefficient with mean ice thickness at each ice station

Freeboard		Surface elevation		Snow depth		Ts	Ti	Basal salinity
mean	s.d.	mean	s.d.	mean	s.d.	mean	mean	mean
0.43	0.86	0.78	0.67	0.82	0.82	0.11	0.04	-0.65

(*) Freeboard is the height of ice surface, while surface elevation is the height of snow surface. T_s is the surface temperature of snow, while T_i is the interface temperature between snow and ice.

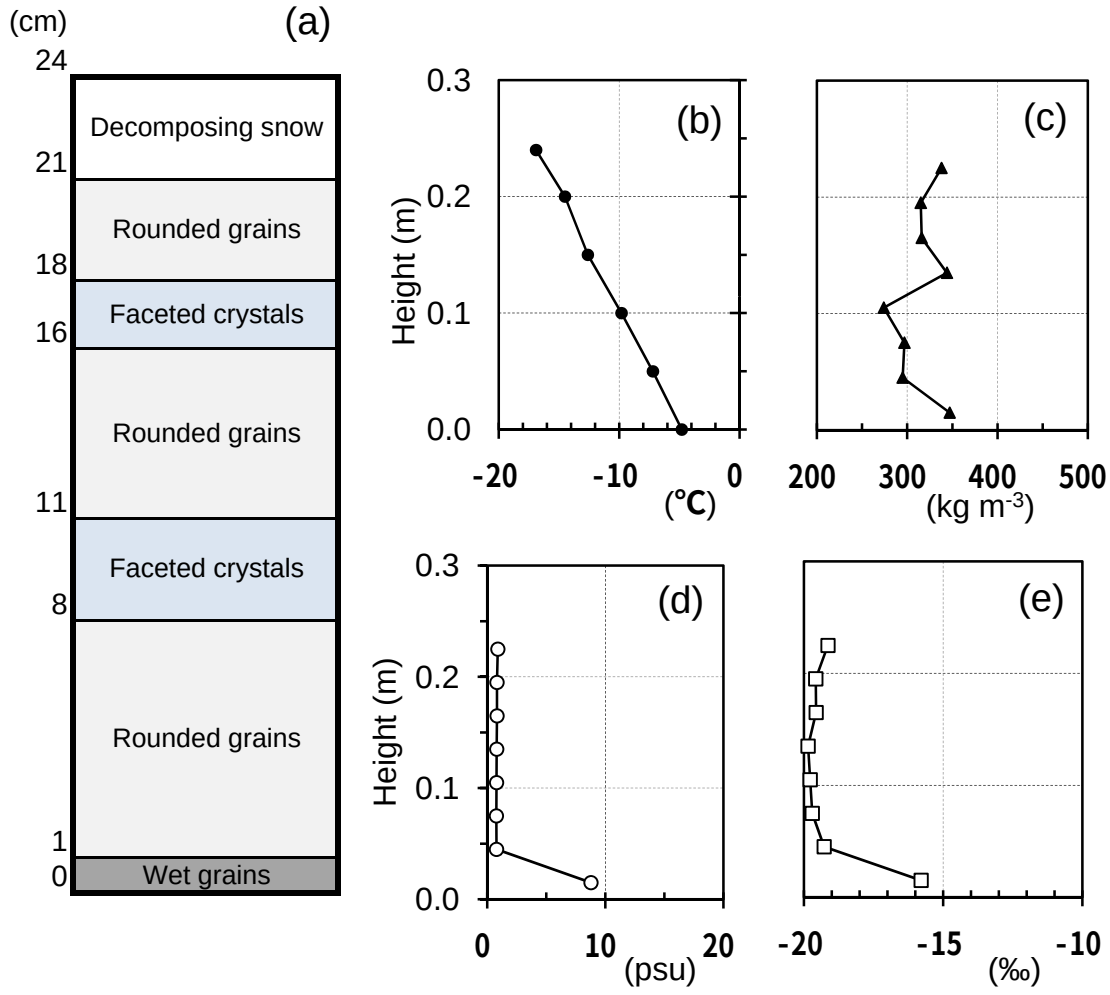
(cm)
(a)
24
21
18
16
11
8
1
0
Decomposing snow
Rounded grains
Faceted crystals
Rounded grains
Faceted crystals
Rounded grains
Wet grains
(b)
Height (m)
0.3
0.2
0.1
0.0
-20
-10
0
(°C)
(c)
200
300
400
500
(kg m-3)
(d)
0
10
20
(psu)
(e)
-20
-15
-10
(‰)

Figure 1

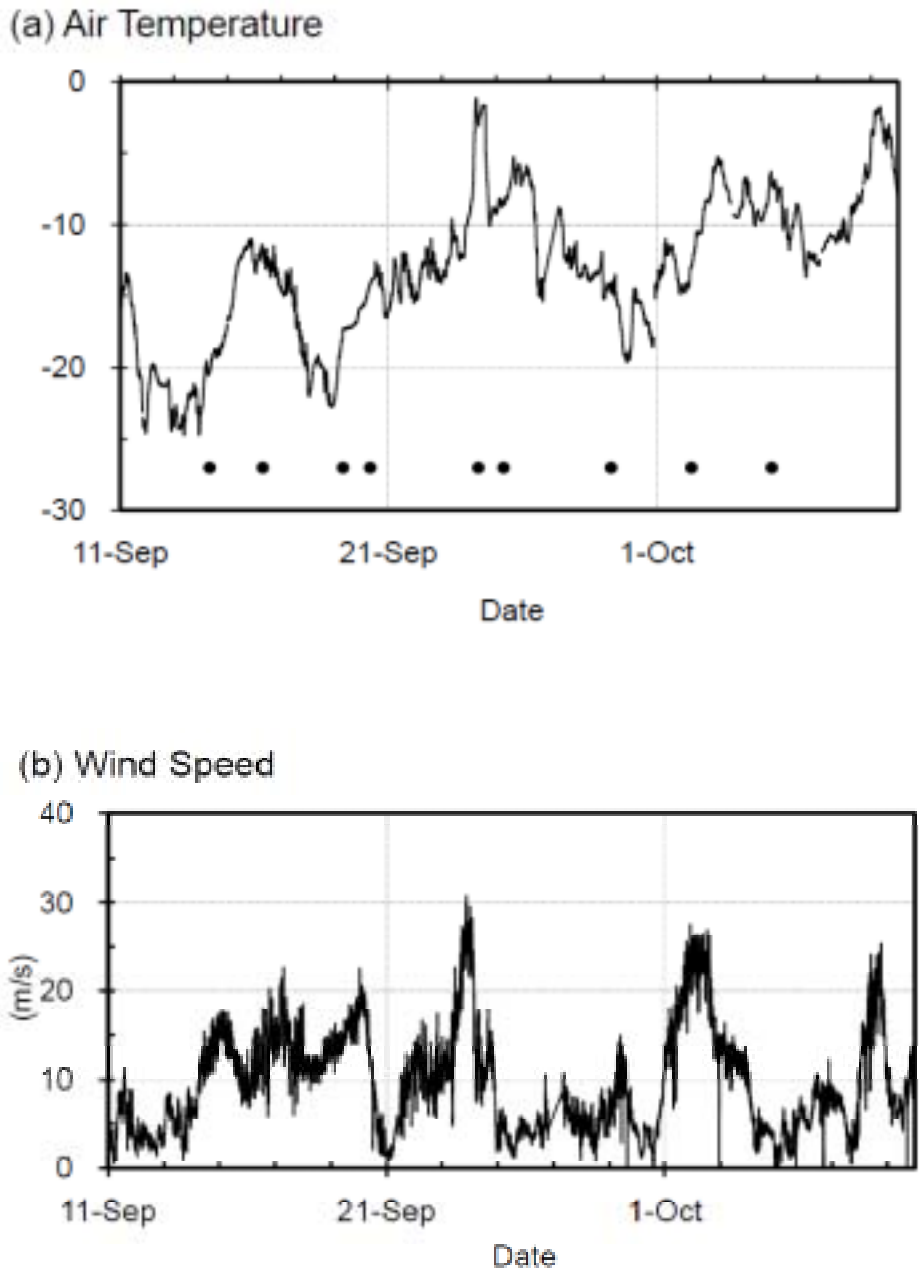
(a) Air Temperature
0
-10
-20
-30
11-Sep
21-Sep
1-Oct
Date
(b) Wind Speed
40
30
20
10
0
(m/s)
11-Sep
21-Sep
1-Oct
Date

Figure 2

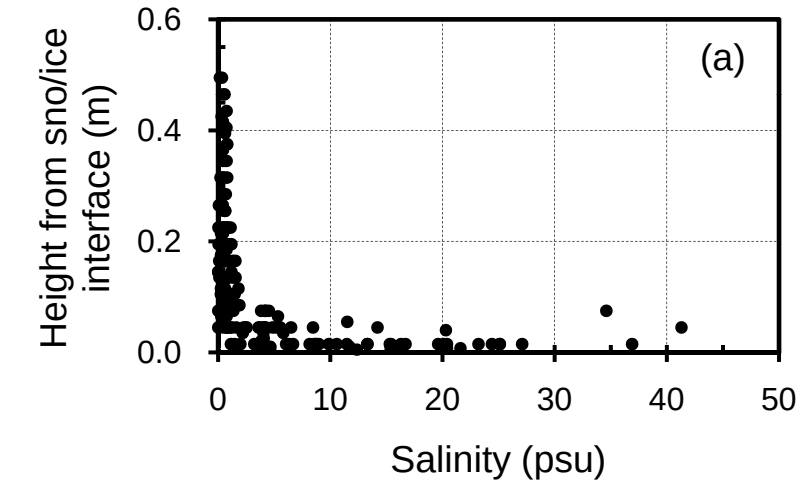
(a)
Height from sno/ice interface (m)
0.6
0.4
0.2
0.0
0
10
20
30
40
50
Salinity (psu)

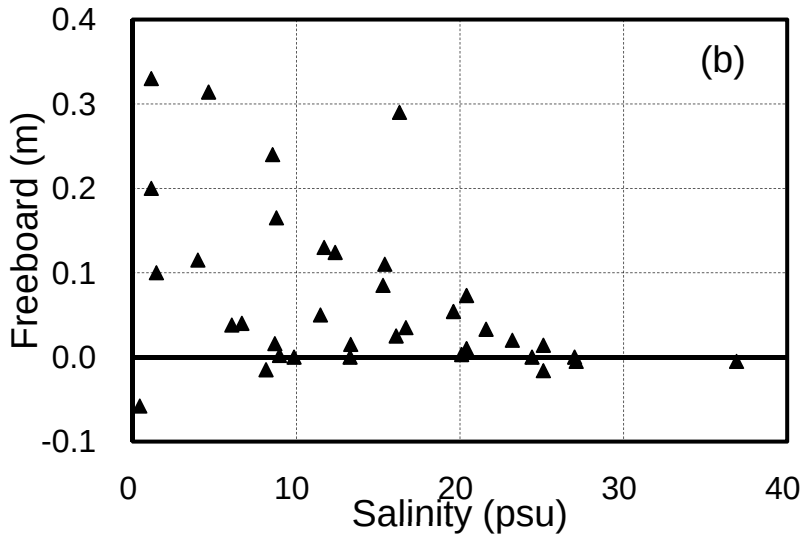
(b)
Freeboard (m)
0.4
0.3
0.2
0.1
0.0
-0.1
0
10
20
30
40
Salinity (psu)

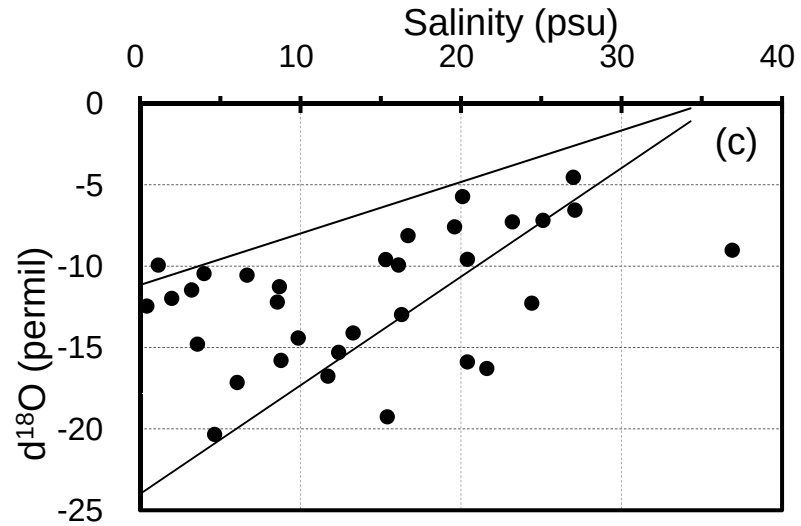
Salinity (psu)
0
10
20
30
40
(c)
d18O (permil)
0
-5
-10
-15
-20
-25

Figure 3

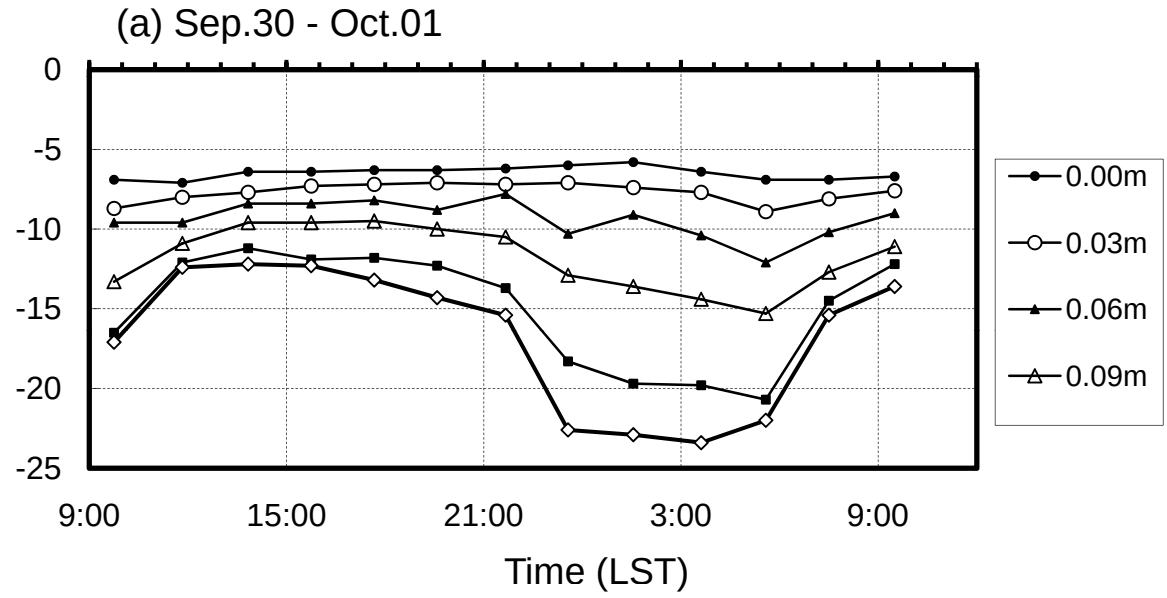
(a) Sep.30 - Oct.01
0
-5
-10
-15
-20
-25
9:00
15:00
21:00
3:00
9:00
Time (LST)
0.00m
0.03m
0.06m
0.09m

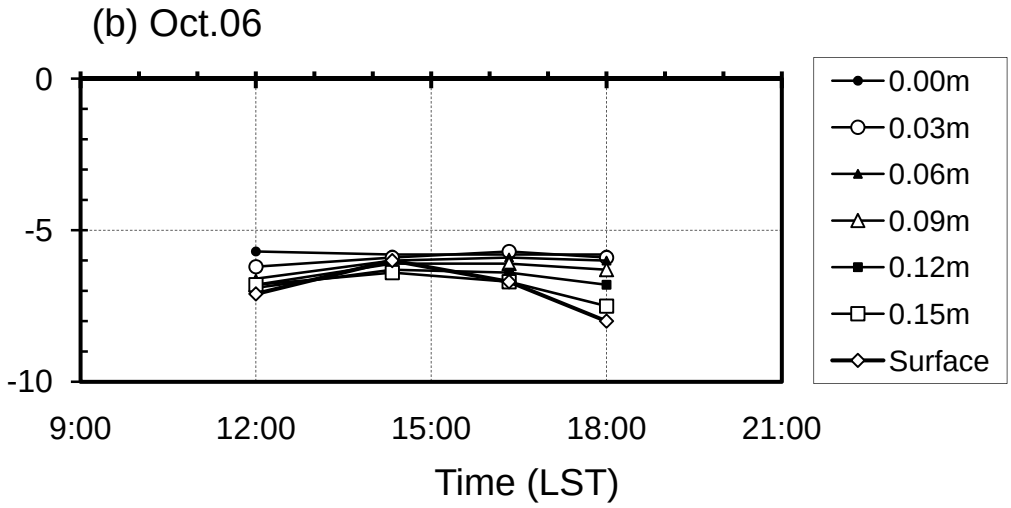
(b) Oct.06
0
-5
-10
9:00
12:00
15:00
18:00
21:00
Time (LST)
0.00m
0.03m
0.06m
0.09m
0.12m
0.15m
Surface

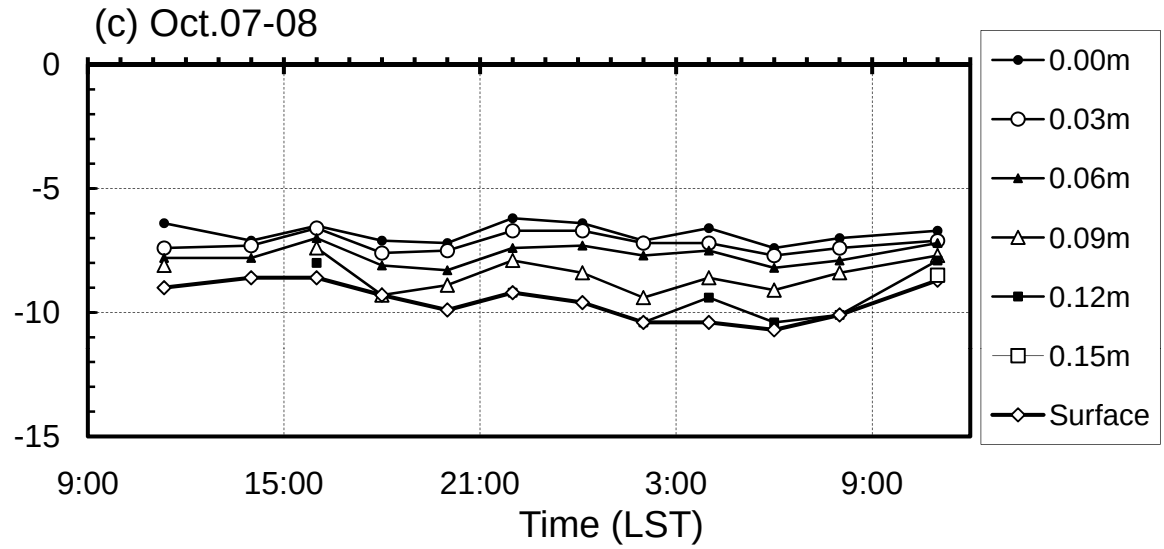
(c) Oct.07-08
0
-5
-10
-15
9:00
15:00
21:00
3:00
9:00
Time (LST)
0.00m
0.03m
0.06m
0.09m
0.12m
0.15m
Surface

Figure 4

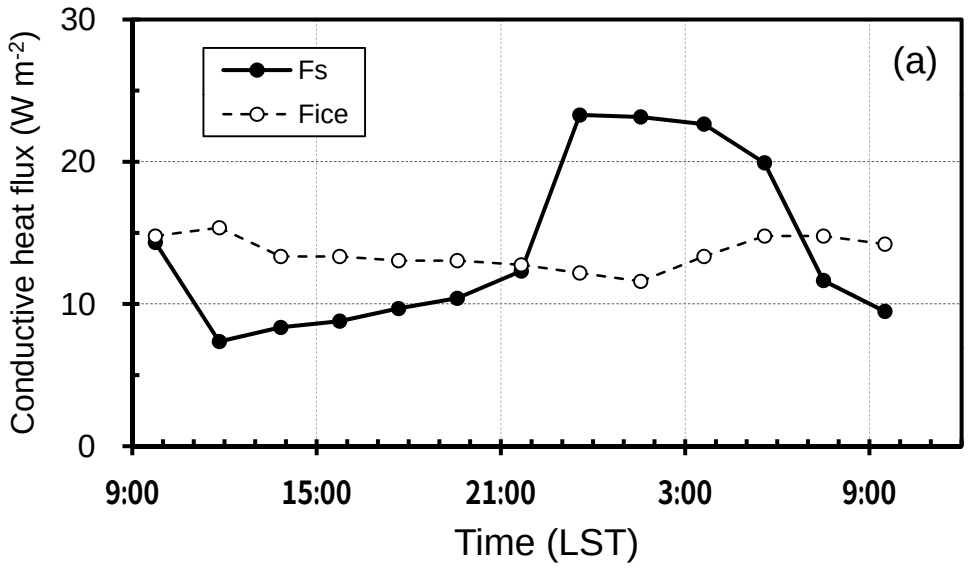
30
20
10
0
Conductive heat flux (W m-2)
Fs
Fice
(a)
9:00
15:00
21:00
3:00
9:00
Time (LST)

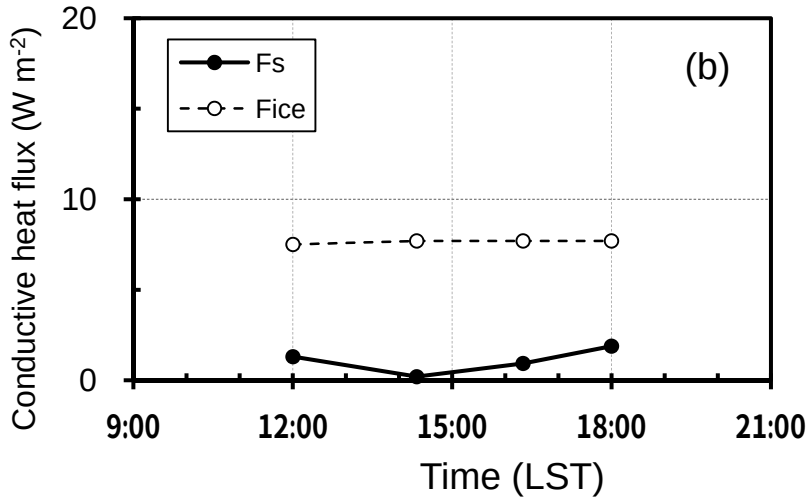
20
10
0
Conductive heat flux (W m-2)
Fs
Fice
(b)
9:00
12:00
15:00
18:00
21:00
Time (LST)

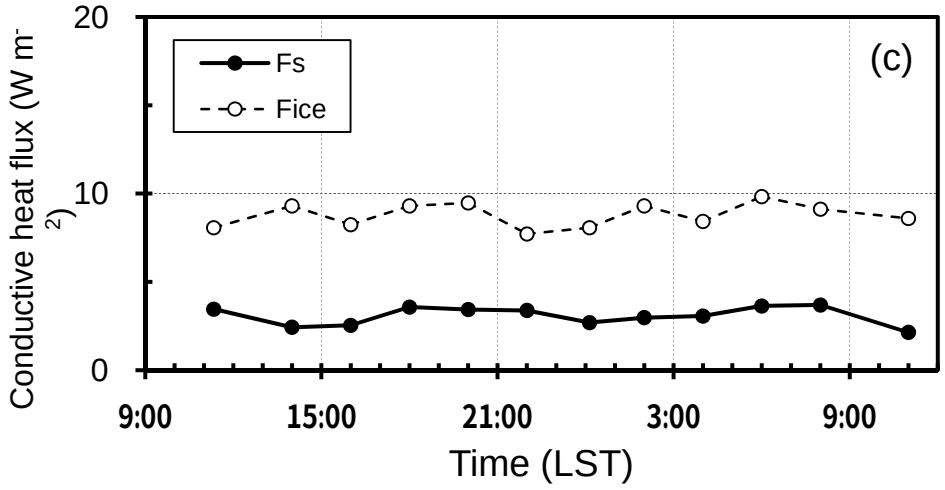
20
10
0
Conductive heat flux (W m-2)
Fs
Fice
(c)
9:00
15:00
21:00
3:00
9:00
Time (LST)

Figure 5

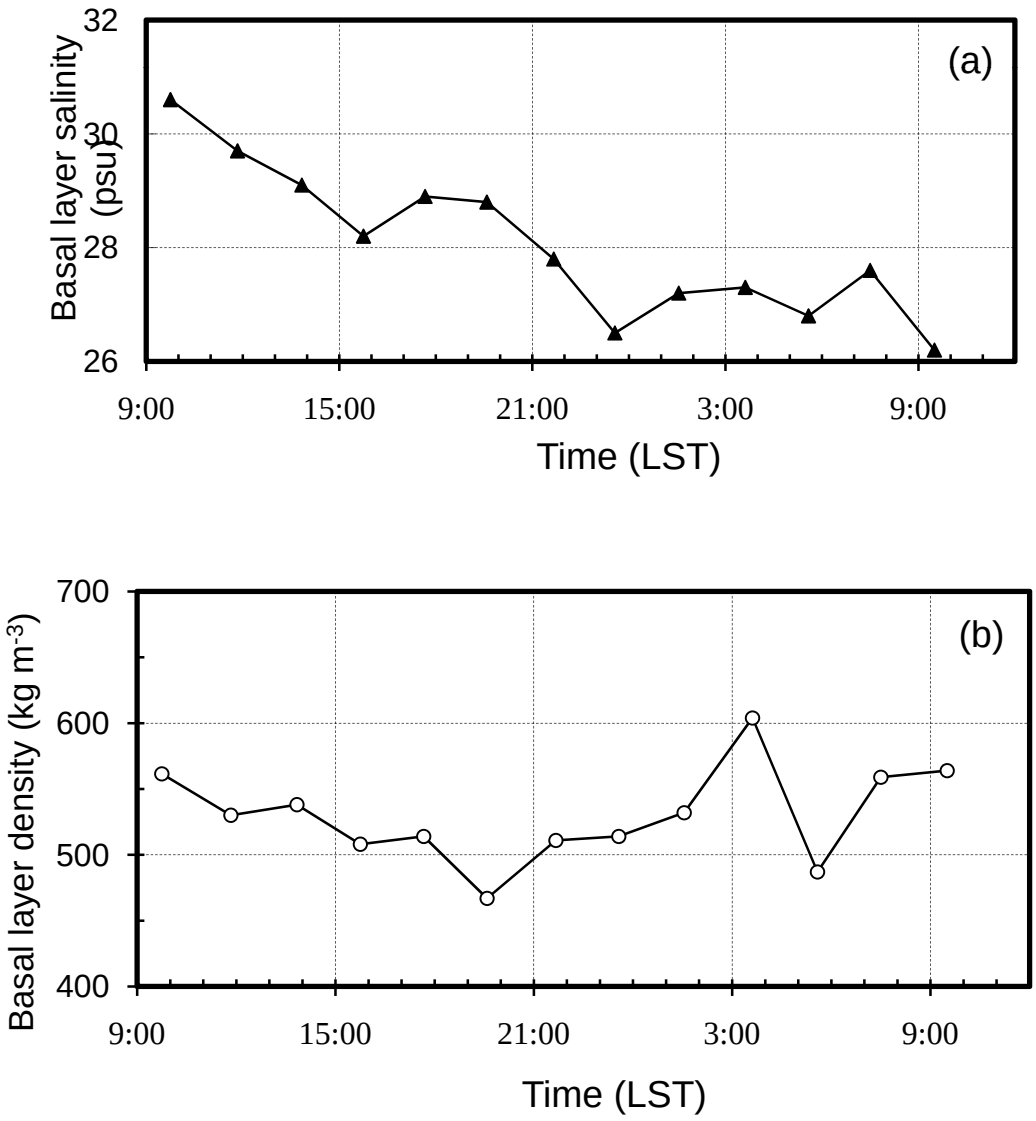
(a)
Basal layer salinity (psu)
32
30
28
26
9:00
15:00
21:00
3:00
9:00
Time (LST)
(b)
Basal layer density (kg m-3)
700
600
500
400
9:00
15:00
21:00
3:00
9:00
Time (LST)

Figure 6

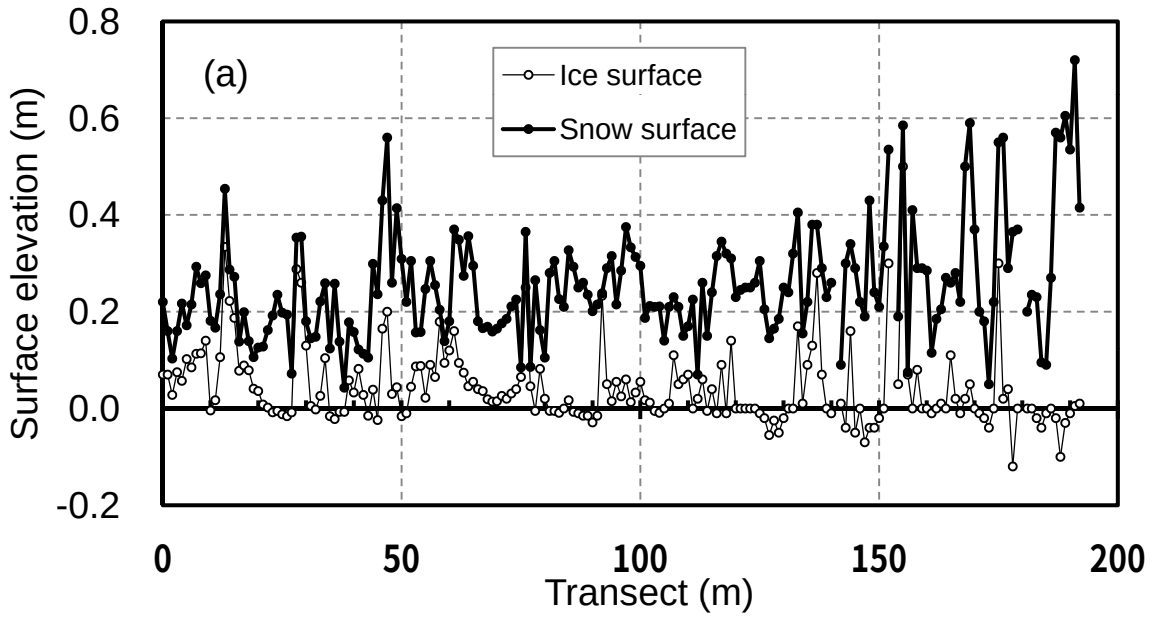
(a)
Ice surface
Snow surface
Surface elevation (m)
0.8
0.6
0.4
0.2
0.0
-0.2
0
50
100
150
200
Transect (m)

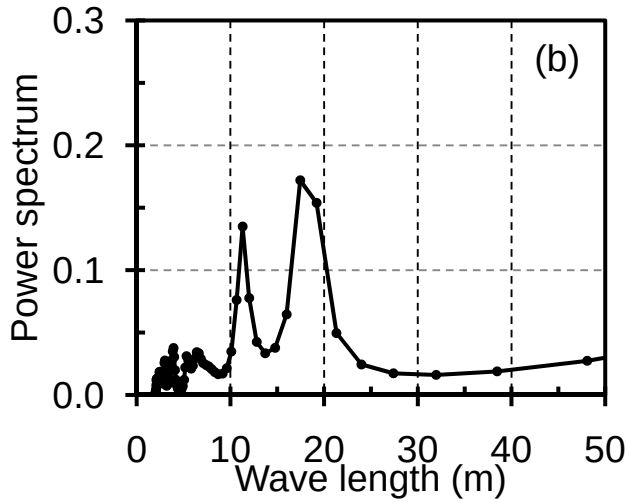
(b)
Power spectrum
0.3
0.2
0.1
0.0
0
10
20
30
40
50
Wave length (m)

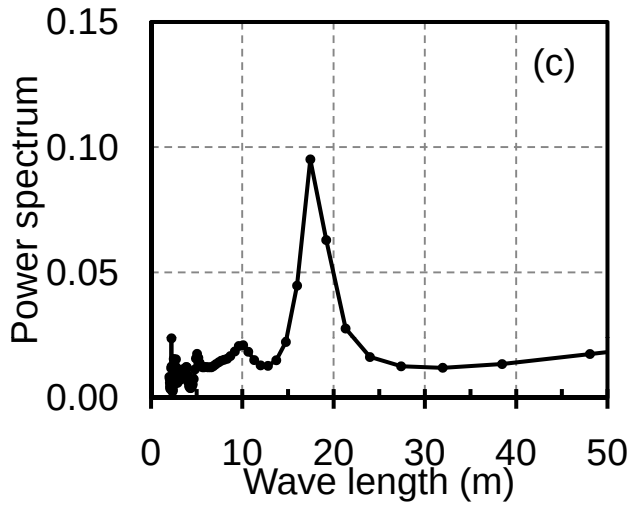
(c)
Power spectrum
0.15
0.10
0.05
0.00
0
10
20
30
40
50
Wave length (m)

Figure 7

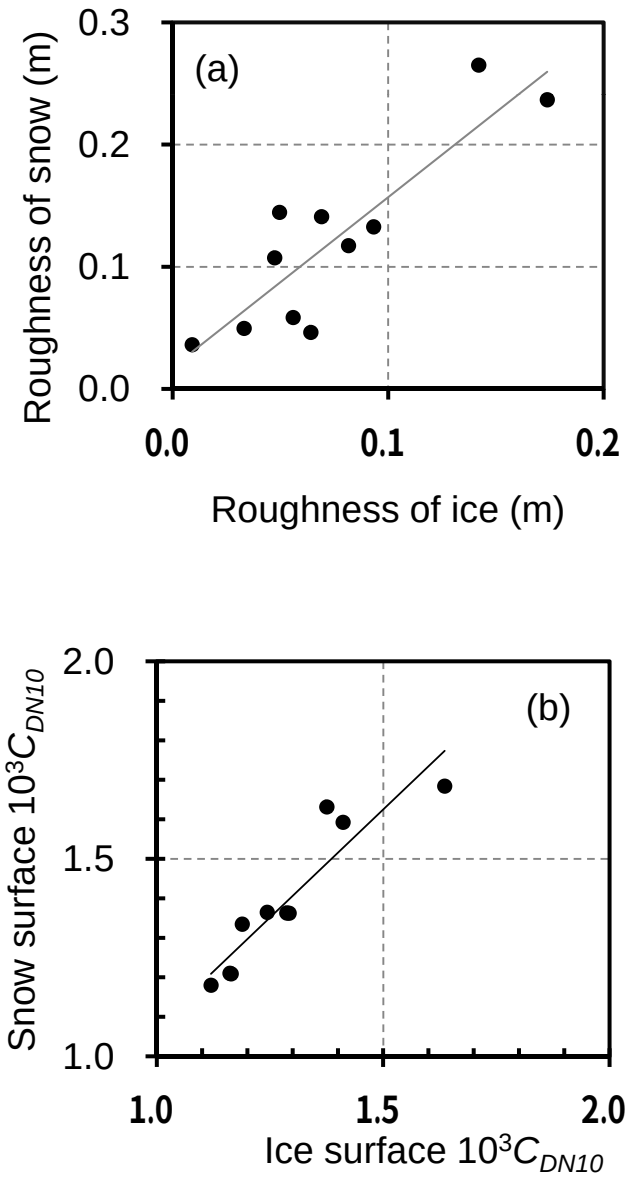
(a)
Roughness of snow (m)
0.3
0.2
0.1
0.0
0.0
0.1
0.2
Roughness of ice (m)
(b)
Snow surface 10^3C_{DN10}
2.0
1.5
1.0
1.0
1.5
2.0
Ice surface 10^3C_{DN10}

Figure 8

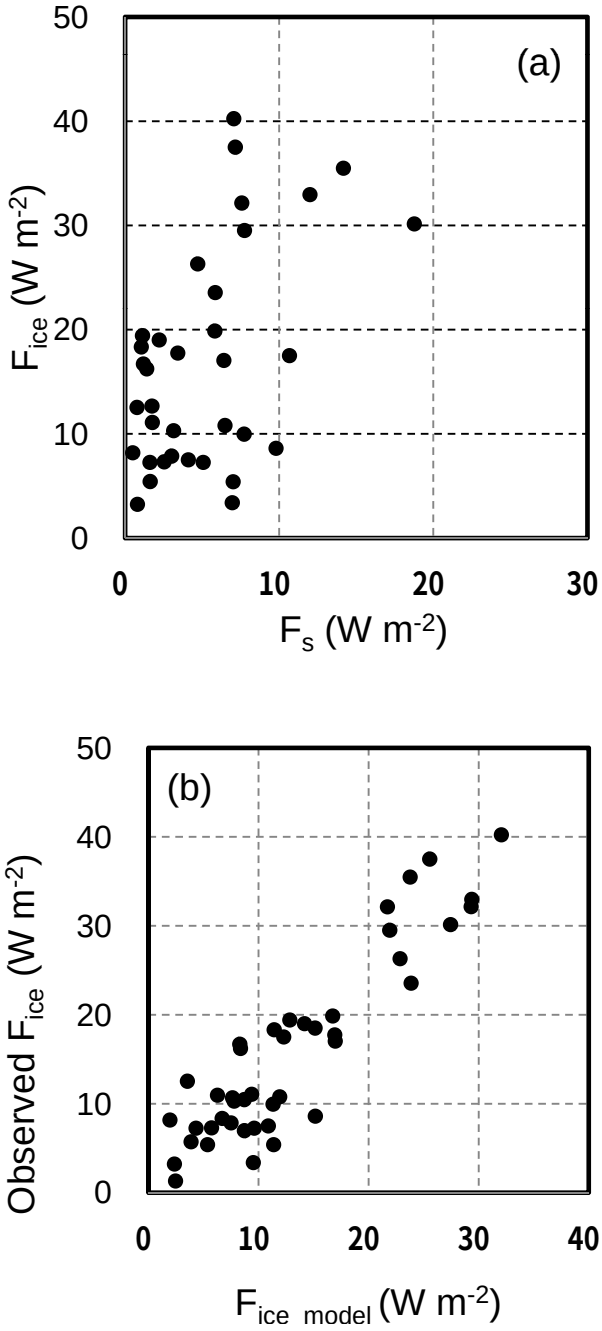
(a)
50
40
30
20
10
0
F_{ice} (W m^{-2})
0
10
20
30
F_s (W m^{-2})
(b)
50
40
30
20
10
0
Observed F_{ice} (W m^{-2})
0
10
20
30
40
$F_{ice\ model}$ (W m^{-2})

Figure 9

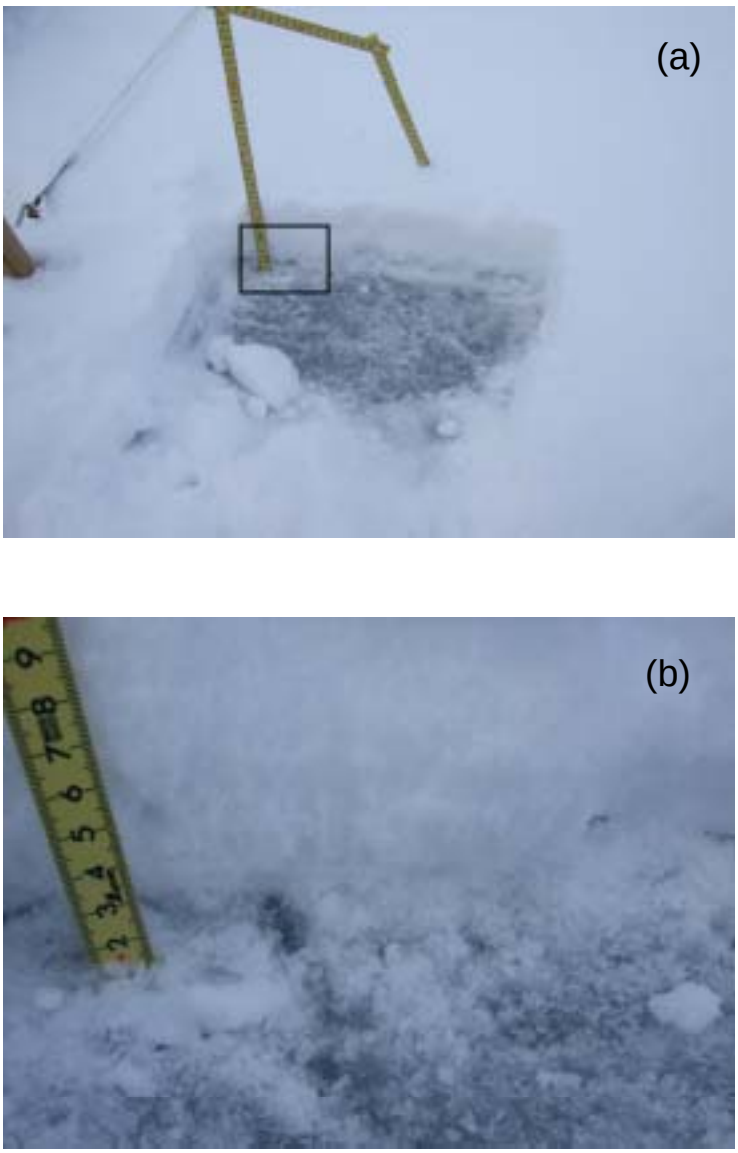

Figure 10

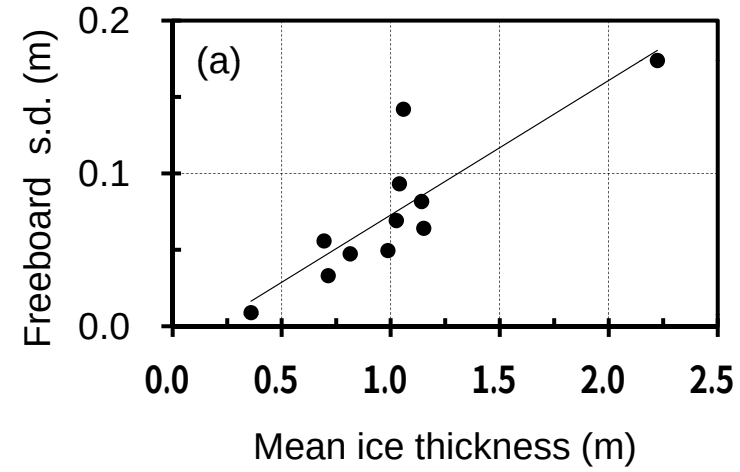
(a)
Freeboard s.d. (m)
0.2
0.1
0.0
0.0
0.5
1.0
1.5
2.0
2.5
Mean ice thickness (m)

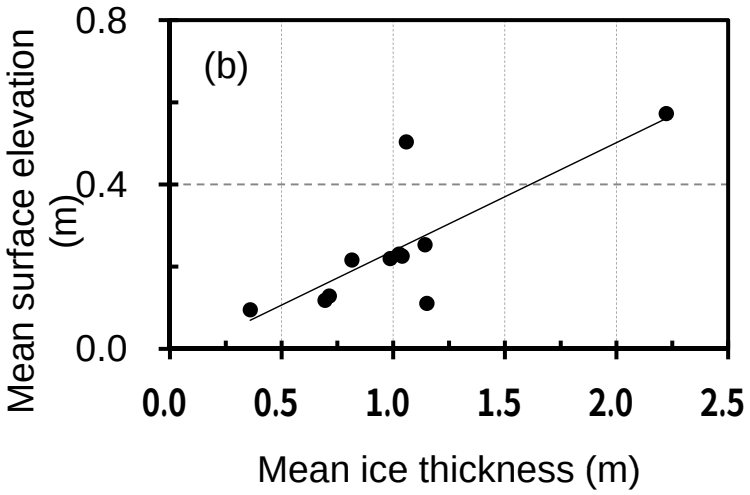
(b)
Mean surface elevation (m)
0.8
0.4
0.0
0.0
0.5
1.0
1.5
2.0
2.5
Mean ice thickness (m)

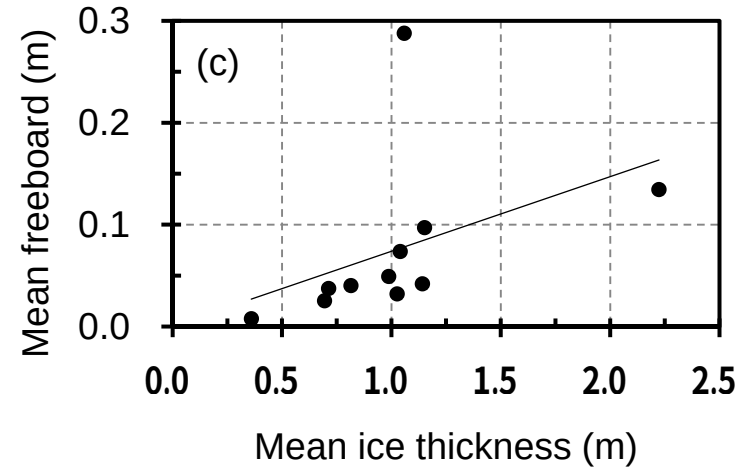
(c)
Mean freeboard (m)
0.3
0.2
0.1
0.0
0.0
0.5
1.0
1.5
2.0
2.5
Mean ice thickness (m)

Figure 11

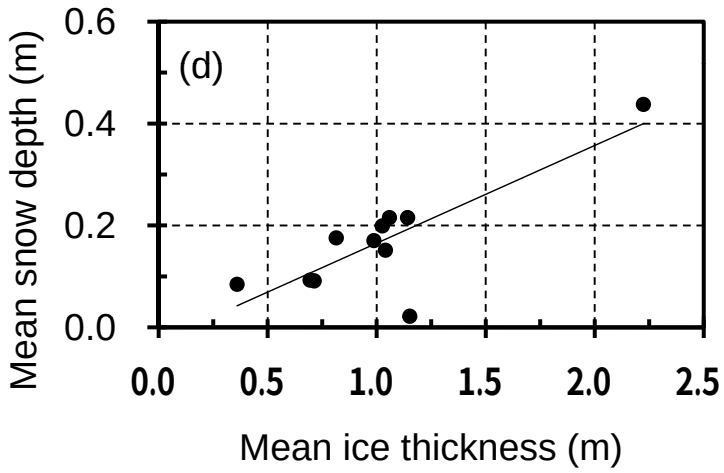
(d)
Mean snow depth (m)
0.6
0.4
0.2
0.0
0.0
0.5
1.0
1.5
2.0
2.5
Mean ice thickness (m)

Figure 11